IEEE Transactions on Quantum Engineering

Received 25 April 2024; revised 18 March 2025; accepted 5 May 2025; date of publication 12 May 2025; date of current version 10 June 2025.

Digital Object Identifier 10.1109/TQE.2025.3569338

Quantum Wavelength-Division Multiplexing and Multiple-Access Communication Systems and Networks: Advanced Applications

MARZIEH BATHAEE[1], MOHAMMAD REZAI[1,2], AND JAWAD A. SALEHI[1,2,3] (Fellow, IEEE)

[1]Sharif Quantum Center, Sharif University of Technology, Tehran 14588-89694, Iran
[2]Center of Quantum Science and Technology, Institute for Convergence Science and Technology, Sharif University of Technology, Tehran 14588-89694, Iran
[3]Electrical Engineering Department, Sharif University of Technology, Tehran 11155-4363, Iran

Corresponding author: Jawad A. Salehi (e-mail: jasalehi@sharif.edu).

ABSTRACT A cost-effective global quantum Internet may be developed using the existing communication infrastructure. This article examines the quantum version of three conventional wavelength-division-multiplexing and multiple-access (WDM) communication systems and networks. They are Lambdanet-based broadcast WDM networks, quantum routers based on a waveguide grating router, and fiber-to-the-quantum nodes that are fed by two opposing and extreme quantum light signals, namely the coherent (Glauber) and number (Fock) states. Using the coherent states, we identify the classical behavior of the quantum WDM (QWDM) networks. Furthermore, employing quantum single-photon sources and exclusive quantum results, such as quantum correlations occurring in the receivers's states, are studied in these WDM communication systems and networks. Finally, we provide secure-key rate estimation for Lambdanet- and waveguide grating router (WGR)-based quantum key distribution networks leveraging the developed QWDM. As compared to Lambdanet, WGR obtains a higher rate of secure keys.

INDEX TERMS All-quantum network, fiber-to-the-quantum nodes (FTTQ), quantum key distribution (QKD), quantum Lambdanet, quantum WDM (QWDM), quantum arrayed waveguide grating, quantum communications, quantum fiber-to-the-home (FTTH), quantum Internet, quantum network, wavelength-division-multiplexing and multiple-access (WDM), wavelength-division multiple-access, wavelength-division multiplexing.

I. INTRODUCTION

Due to the unprecedented amount of information and high-speed communications, communication networks require more strict security measures. The conventional utilized network security is based on computational complexity facing the constant threat of hacking. An unconditional-secured quantum communication network can overcome this weakness once and forever [1]. Furthermore, the advanced forms of upcoming quantum technologies, such as quantum communications [2], [3], [4], quantum computations [5], [6], quantum teleportations [7], [8], and quantum metrologies [9] require quantum networks that pave the way for a futuristic quantum Internet [10], [11], [12].

In present-day communication systems, using wavelength-division-multiplexing and multiple-access (WDM) techniques results in an all-optical network technology in which the wavelength of each channel is used to switch, route, or distribute each channel to its desired location. As a result, we recently examined quantum multiaccess WDM communication systems (QWDM) [13]. For this purpose, a systematic approach to the generic quantum signals evolving from WDM instruments was developed. Moreover, the quantum operations of transmitters, passive wavelength distributors, and receivers in a general WDM quantum communication system were analyzed. Employing the general results of [13], we rigorously examine some popular passive

wavelength distributors in a fully quantum context in this article.

In conventional WDM networks, broadcast-and-select (B&S) networks and wavelength-routed networks (WRN) are the two most commonly used types of WDM architectures [14], [15]. One of the well-known examples of single-hop B&S networks is the Lambdanet network [16]. The Lambdanet utilizes a star coupler as a passive node to distribute a signal equally to all the links. Since the network utilizes the passive node, it becomes reliable and cost-effective compared with its active counterparts. However, this scheme has drawbacks, such as the lack of wavelength reuse and power splitting loss. The loss problem in the Lambdanet can be solved by substituting the star coupler with a waveguide grating router (WGR) employed in WRN-based topologies. In addition, WRN architectures allow reusing wavelengths in WDM networks. Note that different topologies can be employed depending on communication distances and the number of network users. For instance, in short distances, an optical access network connects a service provider (central office) to local clients (subscribers). A so-called fiber-to-the-home (FTTH) topology is typical for transmitting signals from the central office (hub) to the remote node and individual end-users via wavelength multiplexing and demultiplexing.

Modern optical networks enable high-speed data transmission over long distances using key components, such as optical fibers, transmitters and receivers, wavelength-division multiplexers (WDM), optical amplifiers, and switches. While classical networks rely on optical amplifiers to boost signals over long distances, the no-cloning theorem prevents amplification in quantum networks, and amplifiers introduce excess noise to quantum signals. As a result, one strategy for integrating quantum communication is bypassing amplifiers and optimizing loss management. This work provides a mathematical quantum model of all passive WDM components, where fiber losses are modeled using beam splitters (BS) to accurately characterize quantum signal evolution in hybrid quantum-classical networks.

Since future networking relies on the quantum properties of light, several attempts have already been conducted to investigate the quantum version of the WDM networks, as mentioned above. Currently, a significant part of these efforts has been concentrated on the quantum key distribution (QKD) application in a WDM network [17], [18], [19], [20], [21], [22] and the consolidation of classical and quantum signals in the existing infrastructures [23], [24], [25], [26], [27], [28], [29], [30]. Recent advancements have focused on integrating QKD with existing wavelength-division multiplexing (WDM) infrastructures to facilitate the copropagation of quantum and classical signals. A notable study [31] investigates the viability of transmitting weak quantum signals alongside strong classical data traffic within the same optical fiber. The research highlights that crosstalk primarily affects channels adjacent to the classical signal, suggesting that WDM is inherently robust for integrating quantum links into classical networks. For instance [32] and [33] have shown, by an optimum opting of channel spacing, bandwidth filtering, and classical light launch power, the advert effect of classical signals on weak quantum signals will be diminished. Thus, QWDM networks can be studied in a relatively good approximation by examining isolated quantum light signals through the network. Generally, a point-to-point QKD protocol is categorized into two classes, i.e., prepare & measure and entanglement-based protocols. Accordingly, wide, metropolitan, and local area WDM networks for QKD have been demonstrated for both classes [34], [35], [36].

This article builds upon the foundational work presented in [13], where a general QWDM distributor was investigated. We extend this analysis by exemplifying three well-known WDM network architectures—Lambdanet, WGR-based, and FTTH—within a quantum framework. Specifically, we present a detailed mathematical quantum model for these architectures, enabling the study of quantum signal evolution in realistic network settings. In particular, for the first time, we provide a quantum mathematical model for FTTH, referred to as fiber to the quantum (FTTQ), in this work. Furthermore, our results offer a practical framework for characterizing key WDM component parameters, which is essential for optimizing their performance in quantum networks. Through these three specific communication systems, we study the evolution of coherent signals as the output of conventional laser sources and single-photon signals as purely quantum sources. While challenges in scaling and integrating quantum single-photon sources persist, recent advancements offer optimism. Notably, coupling single-photon emitters with designer nanostructures has significantly enhanced emission performance, a crucial step toward the practical implementation of large-scale quantum networks [37]. Developing photonic quantum chips made from glass has also led to more efficient and environmentally friendly quantum systems operating effectively at room temperature [38]. These innovations suggest that practical, large-scale quantum photonic networks may be achievable in the near future. Finally, as a benchmark application of QWDM networks, QKD networks based on the Lambdanet and WGR schemes are compared. Managing and optimizing the performance of complex QWDM networks necessitates substantial research, development, and practical experimentation. This process involves addressing challenges, such as signal loss, crosstalk, and the integration of quantum and classical channels. This work contributes to this endeavor by offering a mathematical model that aids in understanding and mitigating these complexities. We hope this model serves as a foundation for future research aimed at enhancing the performance and scalability of QWDM networks.

The rest of this article is organized as follows. We review the main results of the previous work on generic QWDM systems [13] used in this article, in Section II. Section III is dedicated to exploring a quantum version of the Lambdanet WDM network fed by coherent or single-photon signals. In Section IV, we utilize a wavelength grating router to

IEEE Transactions on Quantum Engineering

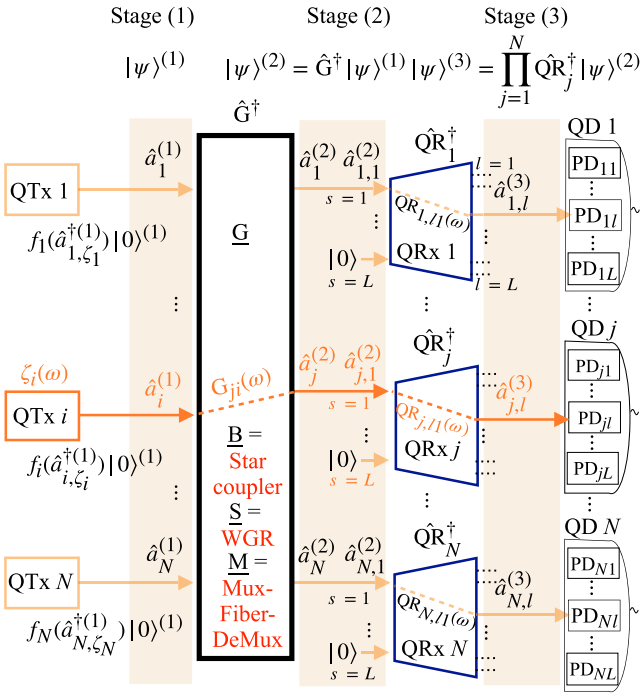

FIGURE 1. Schematic configuration of a generic Quantum Wavelength Division Multiplexing Network. Depending on the chosen network topology, the unitary operator $\hat{\mathbf{G}}^{\dagger}$ will be replaced by a star coupler (**B**), a combination of multiplexer/fiber/demultiplexer (**M**), or a wavelength grating router (WGR) (**S**). Quantum transmitters (QTx) can be narrow and/or broadband lasers or single-photon sources. Input signals can be either weak-coherent or single-photon pulses. Quantum receivers (QRx), depending on a particular choice of **G**, are a demultiplexer and/or a single frequency filter. Quantum detectors ($\mathbf{QD_j}$) holds L photodetectors, i.e., $\mathbf{PD_{jl}}$, $\mathbf{l = 1, \ldots, L}$.

investigate a low-loss, fully connected QWDM network. Section V specifically studies the quantum version of the essential and well-known FTTH WDM topology (FTTQ), where senders emit coherent and single-photon signals. The secure key rate achieved in the polarization-based BB84 QKD protocol [39] is scrutinized via two topologies based on the star coupler and WGR in Section VI. Finally, Section VII concludes this article.

II. ALL-QUANTUM GENERIC QWDM SYSTEM

A generic WDM communication system comprises N transmitters and N receivers, where signals carrying information are distributed to the network via wavelength distributors. Accordingly, as depicted in Fig. 1, generic quantum WDM communication systems and networks introduce three main stages for quantum signals transmitting from N quantum transmitters (QTx) to N quantum receivers (QRx) [13]. Fig. 1 illustrates the evolution of the quantum light state at each stage of a generic QWDM network before entering the next stage. The encoding strategies followed by this article are based on state preparation and measurement. Therefore, no entanglement source is assumed to be used by transmitters. Since different quantum sources can be employed in the QWDM, quantum input light signals are defined as source-specified functions of the creation operators $\hat{a}^{\dagger}_{i,\zeta_i} = \int d\omega \zeta_i(\omega)\hat{a}^{\dagger}_i(\omega)$ with wave-packet $\zeta_i(\omega)$ relating to the ith quantum source. Thus, the tensor product of the pure input state signal emitted by the user's transmitters in stage (1) is expressed as

$$|\psi\rangle^{(1)} = \prod_{i=1}^{N} |\psi_{\zeta_i}\rangle^{(1)} = \prod_{i=1}^{N} f_i(\hat{a}^{\dagger(1)}_{i,\zeta_i})|0\rangle^{(1)} \tag{1}$$

where $f_i(\hat{a}^{\dagger(1)}_{i,\zeta_i})|0\rangle = \sum_{n=0}^{\infty} \frac{c_n}{\sqrt{n!}} \hat{a}^{\dagger(1)^n}_{i,\zeta_i}|0\rangle$ and f_i is a normalized analytical function. The signal $|\psi\rangle^{(1)}$ evolves through the following quantum operators: first, a global wavelength distributor $\hat{\mathrm{G}}^{\dagger}$ (i.e., $|\psi\rangle^{(2)} = \hat{\mathrm{G}}^{\dagger}|\psi\rangle^{(1)}$) and then the product of local QRx operators, i.e., $\hat{\mathrm{QR}}^{\dagger} = \prod_{j=1}^{N} \hat{\mathrm{QR}}^{\dagger}_j$ ($|\psi\rangle^{(3)} = \hat{\mathrm{QR}}^{\dagger}|\psi\rangle^{(2)}$). As a result, the final state becomes

$$\begin{aligned} |\psi\rangle^{(3)} &= \hat{\mathrm{QR}}^{\dagger}|\psi\rangle^{(2)} = \hat{\mathrm{QR}}^{\dagger}\hat{\mathrm{G}}^{\dagger}|\psi\rangle^{(1)} \\ &= \prod_{i=1}^{N} f_i(\hat{\mathrm{QR}}^{\dagger}\hat{\mathrm{G}}^{\dagger}\hat{a}^{\dagger(1)}_{i,\zeta_i}\hat{\mathrm{G}}\hat{\mathrm{QR}})|0\rangle^{(3)} \\ &= \prod_{i=1}^{N} f_i\left(\sum_{j=1}^{N}\sum_{l=1}^{L} \mathcal{M}_{lsji}\hat{a}^{\dagger(3)}_{j,l,\gamma_{lsji}}\right)|0\rangle^{(3)}. \end{aligned} \tag{2}$$

In the last line of (2), we utilize the input–output mode relation [13], [40] due to the unitary evolution $\hat{\mathrm{QR}}^{\dagger}\hat{\mathrm{G}}^{\dagger}$, where

$$\mathcal{M}_{lsji} = \mathrm{G}_{ji}(\zeta_i)\mathrm{QR}_{j,ls}(\eta_{ji}) \tag{3}$$

$$\eta_{ji}(\omega) = \zeta_i(\omega)\mathrm{G}_{ji}(\omega)/\mathrm{G}_{ji}(\zeta_i) \tag{4}$$

$$\gamma_{lsji}(\omega) = \eta_{ji}(\omega)\mathrm{QR}_{j,ls}(\omega)/\mathrm{QR}_{j,ls}(\eta_{ji}) \tag{5}$$

$$\hat{a}^{\dagger(3)}_{j,l,\gamma_{lsji}} = \int d\omega \gamma_{lsji}(\omega)\hat{a}^{\dagger(3)}_{j,l}(\omega) \tag{6}$$

and L is the number of QRx input/output ports, as shown in Fig. 1. In (3), $\mathrm{G}_{ji}(\zeta_i)$ is the norm of the weighted wave-packet $\zeta_i(\omega)\mathrm{G}_{ji}(\omega) = \mathrm{G}_{ji}(\zeta_i)\eta_{ji}(\omega)$ produced after signals pass through $\hat{\mathrm{G}}^{\dagger}$, and $\mathrm{QR}_{j,ls}(\eta_{ji})$ is the norm of the weighted wave-packet $\eta_{ji}(\omega)\mathrm{QR}_{j,ls}(\omega) = \mathrm{QR}_{j,ls}(\eta_{ji})\gamma_{lsji}(\omega)$ generated after signal evolution by $\hat{\mathrm{QR}}^{\dagger}_j$. In other words, in (4) and (5), $\eta_{ji}(\omega)$ and $\gamma_{lsji}(\omega)$ are the normalized wave packets of signals after evolution by the global operator $\hat{\mathrm{G}}^{\dagger}$ and the local operators $\hat{\mathrm{QR}}^{\dagger}_j$. Therefore, the probability amplitude that the signal with the wave-packet $\zeta_i(\omega)$ arrives at the lth output port of the jth receiver, indicated by the photodetector PD_{jl} in Fig. 1, becomes

$$\bar{\gamma}_{lsji}(\omega) = \mathcal{M}_{lsji}\gamma_{lsji}(\omega) = \mathrm{QR}_{j,ls}(\omega)\mathrm{G}_{ji}(\omega)\zeta_i(\omega). \tag{7}$$

The QRx are usually demultiplexers, mathematically modeled by $N \times N$ unitary operators where only one input is fed by received signals. The passing frequency from input port s to output port l of the QRx is indicated by ω_{ls}. The quantum

network topologies presented in this article consider single-photon and coherent states as input signals. As a result, the essential results corresponding to these two input states are summarized in the following subsections. For more detailed information see [13, Sec. IV].

A. COHERENT STATE INPUTS

The functionality of f_i on the creation operator presented in (1), for coherent state inputs, is

$$f_i(\hat{a}^{\dagger(1)}_{i,\zeta_i})|0\rangle = \hat{D}(\alpha_i\zeta_i)|0\rangle \tag{8}$$

where $\hat{D}(\alpha_i\zeta_i) = \exp(\alpha_i\hat{a}^{\dagger(1)}_{i,\zeta_i} - \alpha^*_i\hat{a}^{(1)}_{i,\zeta_i})$ is the displacement operator and α_i is the amplitude of the ith coherent light source (laser).

Using (2) and (8), if all input signals are coherent states, the state at stage (3) becomes a separable state as

$$|\psi\rangle^{(3)}_{\mathrm{C}} = \prod_{i,j,l=1}^{N,N,L} \hat{D}(\alpha_i\bar{\gamma}_{lsji})|0\rangle^{(3)} \tag{9}$$

where $\bar{\gamma}_{lsji}$ is introduced in (7). The spectral intensity of photon at an arbitrary frequency ω acquired by use of the photodetector PD_{jl} (at the lth output of the jth receiver) is

$$\begin{aligned} I_{jl}(\omega) &= {}^{(3)}_{\mathrm{C},jl}\langle\psi|\hat{a}^{\dagger(3)}_{j,l}(\omega)\hat{a}^{(3)}_{j,l}(\omega)|\psi\rangle^{(3)}_{\mathrm{C},jl} \\ &= \left|\sum_{i=1}^{N}\alpha_i\mathrm{QR}_{j,ls}(\omega)\mathrm{G}_{ji}(\omega)\zeta_i(\omega)\right|^2. \end{aligned} \tag{10}$$

Note that the output state (9) is a separable (unentangled) state, thus the state at output port jl becomes the coherent state as

$$|\psi\rangle^{(3)}_{\mathrm{C},jl} = \hat{D}\left(\sum_{i=1}^{N}\alpha_i\bar{\gamma}_{lsji}\right)|0\rangle^{(3)}. \tag{11}$$

Note that

$$\hat{D}\left(\sum_{i=1}^{N}\alpha_i\bar{\gamma}_{lsji}\right) = \exp\left(\sum_{i=1}^{N}\alpha_i\mathcal{N}_{lsji}\hat{a}^{\dagger(1)}_{j,l,\gamma_{lsji}} - h.c\right). \tag{12}$$

B. SINGLE-PHOTON STATE INPUTS

For single-photon state inputs, f_i is obtained as

$$f_i(\hat{a}^{\dagger(1)}_{i,\zeta_i})|0\rangle = \hat{a}^{\dagger(1)}_{i,\zeta_i}|0\rangle. \tag{13}$$

Using (2) and (13), the state at stage (3) is written as

$$\begin{aligned} |\psi\rangle^{(3)}_{\mathrm{S}} &= \prod_{i=1}^{N}\left(\sum_{j=1}^{N}\sum_{l=1}^{L}\mathcal{N}_{lsji}\hat{a}^{\dagger(3)}_{j,l,\gamma_{lsji}}\right)|0\rangle^{(3)} \\ &= \prod_{i=1}^{N}\left(\sum_{j=1}^{N}\sum_{l=1}^{L}\int\bar{\gamma}_{lsji}(\omega)\hat{a}^{\dagger(3)}_{j,l}(\omega)\right)|0\rangle^{(3)} \end{aligned} \tag{14}$$

where, in the last line, (6) and (7) is used. A projective measurement on the potentially entangled state (14) can give us helpful information. It is essential to mention that although the practical implementation of a nondemolishing projective measurement is challenging, detecting a photon after passing through the narrowband filter of the output of the QRx via an existing single-photon detector can be conceived as a demolishing projective measurement. In the demolishing projective measurement, the detected photon is absorbed. Nevertheless, the collapsed state related to other receivers before the measurement is the same as what is obtained in a nondemolishing projective measurement.

The projective operator performed on the output port corresponding to index $\tilde{j}\tilde{l}$ at frequency $\omega_{\tilde{l}s}$ is defined by

$$\begin{aligned} \hat{P}_{\tilde{j}\tilde{l}}(\omega_{\tilde{l}s}) &= |1_{\tilde{j}\tilde{l}}(\omega_{\tilde{l}s})\rangle^{(3)(3)}\langle 1_{\tilde{j}\tilde{l}}(\omega_{\tilde{l}s})| \\ &= \hat{a}^{\dagger(3)}_{\tilde{j},\tilde{l}}(\omega_{\tilde{l}s})|0_{\tilde{j}\tilde{l}}(\omega_{\tilde{l}s})\rangle^{(3)(3)}\langle 0_{\tilde{j}\tilde{l}}(\omega_{\tilde{l}s})|\hat{a}^{(3)}_{\tilde{j},\tilde{l}}(\omega_{\tilde{l}s}). \end{aligned} \tag{15}$$

Therefore, the collapsed state of (14) after this projective measurement becomes (see [13, Appendix E])

$$\begin{aligned} &\hat{P}_{\tilde{j}\tilde{l}}(\omega_{\tilde{l}s})|\psi\rangle^{(3)}_{\mathrm{S}} = |1_{\tilde{j}\tilde{l}}(\omega_{\tilde{l}s})\rangle^{(3)} \\ &\otimes\sum_{i'=1}^{N}\bar{\gamma}_{\tilde{l}s\tilde{j}i'}(\omega_{\tilde{l}s})\left\{\prod_{\substack{i=1\\ i\neq i'}}^{N}\sum_{\substack{j=1,l=1\\ (j,l)\neq(\tilde{j},\tilde{l})}}^{N,L}\mathcal{N}_{lsji}\hat{a}^{\dagger(3)}_{j,l,\gamma_{lsji}}\right\}|0\rangle^{(3)}. \end{aligned} \tag{16}$$

In the following sections, first, we study the Lambdanet network that consists of a star coupler ($\underline{\mathrm{B}}$) as a wavelength distributor ($\underline{\mathrm{G}} = \underline{\mathrm{B}}$ in Fig. 1) and wavelength demultiplexers ($\underline{\mathrm{A}_j}$) as QRx ($\underline{\mathrm{QR}_j} = \underline{\mathrm{A}_j}$). Next, a quantum router-based WDM network is studied where its wavelength distributor is mathematically modeled as a lossy arrayed-waveguide grating indicated by $\underline{\mathrm{S}}$ ($\underline{\mathrm{G}} = \underline{\mathrm{S}}$ in Fig. 1). Finally, for the last topology, the FTTQ QWDM network, a wavelength distributor ($\underline{\mathrm{G}} = \underline{\mathrm{M}}$) is the cascade of wavelength multiplexer, fiber link, and wavelength demultiplexer. Note that in all the following network topologies, we assume the received signal enters port s=1 of QRx j (see Fig. 1) unless otherwise stated without loss of generality (see [13, Appendix D] for more details).

III. LAMBDANET BROADCASTING-BASED QWDM NETWORK

Networks that allow direct communication between users without a central office or third party enhance network security. Using a star coupler as a wavelength distributor, the Lambdanet topology [16] enables users to communicate with each other without relying on a third user. Foundational architectures like Lambdanet have significantly influenced the development of contemporary quantum communication systems. Notably, experimental realizations have demonstrated the feasibility of such architectures. For instance, Townsend's 1997 work [41] can be considered an evolution of the Lambdanet concept, as it implemented a multiuser quantum cryptography network using optical fibers.

IEEE Transactions on Quantum Engineering

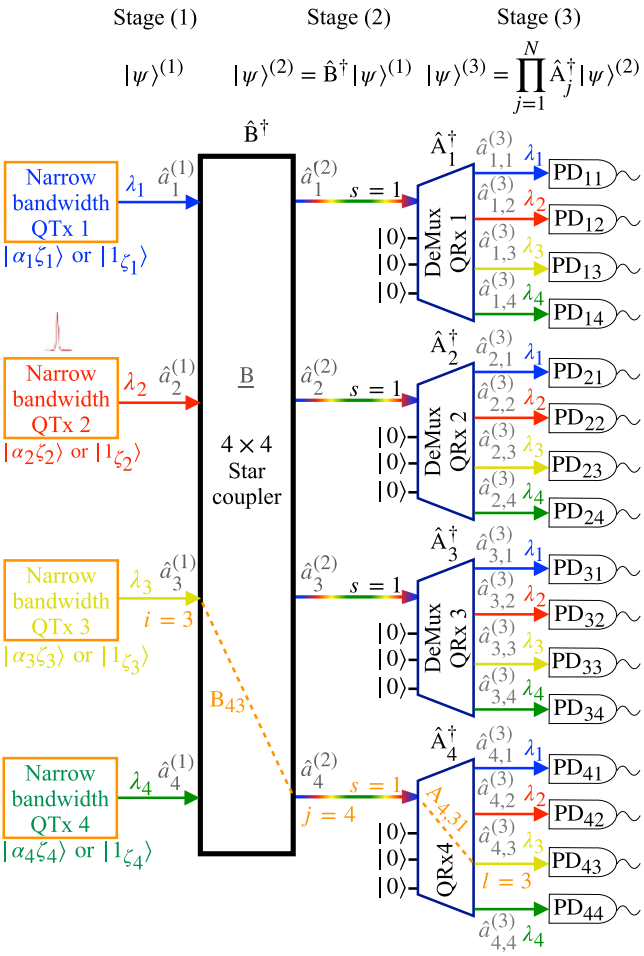

FIGURE 2. Stage (1) four-user quantum Lambdanet network fed by single-photon or coherent state sources.

This study demonstrated the practicality of such architectures in real-world scenarios. In the Lambdanet network depicted in Fig. 2, transmitters' signals are broadcast among all receivers via a star coupler indicated by $\hat{B}^{\dagger}$ ($|\psi\rangle^{(1)} \xrightarrow{\hat{B}^{\dagger}} |\psi\rangle^{(2)} = \hat{B}^{\dagger}|\psi\rangle^{(1)}$, where $\hat{G}^{\dagger} = \hat{B}^{\dagger}$ in (2), (for mathematical modeling of star coupler see Appendix A). Each transmitter, i, transmits the desired information through a quantum state of light composed of narrow frequency band photons expressible as wave-packet $\zeta_i(\omega)$, usually addressed by its central frequency ω_i or wavelength λ_i. A QRx in each receiver's site separates received signals from all transmitters based on their frequency contents employing a wavelength demultiplexer. Assume demultiplexers are arrayed waveguide gratings (AWG) with the linear transfer matrix $\underline{A}$ (see Appendix B). Therefore, the star coupler output signals evolve from stage 2 to stage 3 based on the global unitary operator $\prod_{j=1}^{N} \hat{A}_j^{\dagger}$, where $\hat{A}_j^{\dagger}$ is the local unitary operator related to the jth QRx, i.e., $\hat{QR}_j = \hat{A}_j$ in (2) ($|\psi\rangle^{(2)} \xrightarrow{\prod_{j=1}^{N} \hat{A}_j^{\dagger}} |\psi\rangle^{(3)} = \prod_{j=1}^{N} \hat{A}_j^{\dagger}|\psi\rangle^{(2)}$). The wavelength demultiplexers must at least possess L output ports equal to the number of users (N), $N = L$, to decode any desired sender's information from the received signals. In the Lambdanet topology, every user has a transmitter and a receiver at their disposal. For a frequency-independent star coupler, the state of the QWDM system at stage (3) is acquired by substituting B_{ji} in (2) in place of $G_{ji}(\omega)$. As illustrated in Fig. 2 for a Lambdanet network with $N = 4$, the mathematical models of wavelength demultiplexers as the QRx have $N - 1 = 3$ input ports fed by vacuum states. The symbol s indicates the input ports of the wavelength demultiplexer. As discussed in [13, Appendix D], without loss of generality, the nonvacuum-state fed input port for all the receivers can be labeled by the same s. So, for all j, $\hat{a}_j^{(2)} \equiv \hat{a}_{j,s}^{(2)}$. In addition, for the Lambdanet topology $QR_{j,ls}(\omega)$ is replaced by $A_{j,ls}(\omega)$ in (2)–(7). Fig. 2 illustrates the guided frequency $\omega_{ls} = \omega_{l-s+1 \bmod N}$ by a demultiplexer from its input $s = 1$ to its output l which is denoted by the central wavelength $\lambda_l = 2\pi c/\omega_l$ of the lth transmitted signal. The Lambdanet network is investigated in the following subsections for two kinds of mainstream inputs: 1) coherent states and 2) single-photon states.

A. COHERENT SIGNALS AS INPUTS

Consider that all transmitters emit coherent states. Hence, according to (7) and (10), the spectral intensity detected at the lth output of the jth receiver becomes

$$I_{jl}(\omega_{ls}) = {}^{(3)}_{jl,C}\langle\psi|\hat{a}_{j,l}^{\dagger(3)}(\omega_{ls})\hat{a}_{j,l}^{(3)}(\omega_{ls})|\psi\rangle^{(3)}_{C,jl} = \left|\sum_{i=1}^{N} \alpha_i A_{j,ls}(\omega_{ls}) B_{ji} \zeta_i(\omega_{ls})\right|^2 = \left|\sum_{i=1}^{N} \alpha_i \bar{\gamma}_{lsji}(\omega_{ls})\right|^2. \tag{17}$$

Since the transmitters utilize the narrow-bandwidth sources well separated from each other with respect to their central wavelengths, one can apply the approximation $A_{j,l1}(\omega_{l1})\zeta_i(\omega_{l1}) \approx \delta_{il} A_{j,l1}(\omega_l)\zeta_i(\omega_l)$ (where $s = 1$, $\omega_{l1} = \omega_l$) in (17) to get the result

$$I_{jl}(\omega_{l1}) \approx |\alpha_l B_{jl} A_{j,l1}(\omega_l)\zeta_l(\omega_l)|^2 \ \forall j, l \in \{1, \ldots, N\}. \tag{18}$$

Moreover, according to (11), the state at the output port number l of the jth demultiplexer becomes

$$|\psi\rangle^{(3)}_{C,jl} \approx \hat{D}(\alpha_l \bar{\gamma}_{l1\,jl})|0\rangle^{(3)}. \tag{19}$$

Since only the signal of the lth transmitter indicated by $\zeta_l(\omega_l)$ contributes to the spectral intensity $I_{jl}(\omega_{l1})$, every receiver has access to each transmitted signal individually at its related receiver's output (see for instance path $i = 3 \to j = 4 \to s = 1 \to l = 3$ in Fig. 2). For weak input coherent states, $|\alpha_i|^2 \ll 1$, receivers' single-photon detectors (SPD) click with the probability proportional to $I_{jl}(\omega_{ls})$ in line with the Kelley–Kleiner formula [42]. Apart from the vacuum state existing in the coherent state, the weak coherent source emits a single photon with a higher probability than multi-photon states. So the probability that two different receivers

simultaneously receive the same input signal due to a multiphoton state contribution in the coherent state prepared by the same transmitter is not significant [41]. As a result, secure communication between each pair becomes possible by omitting unsecured data related to these multiphoton signals, e.g., by discarding data resulting from multiphoton states in the postprocessing procedure of decoy state-assisted QKD protocols [43]. Alternatively, one can use an ideal single-photon source to prevent the security issues corresponding to the multiphoton existing in the coherent signals, for instance, in QKD protocols. The operation of Lambdanet topology based on ideal single-photon sources is studied in the sequel.

B. SINGLE-PHOTON SIGNALS AS INPUTS

In contrast to coherent states, transmitting single-photon signals in the network can create an entangled correlated state between receivers. To better understand the operation of the quantum Lambdanet network fed by single-photon sources, the four-user network illustrated in Fig. 2 is considered. The transmitted carrier frequencies dedicated to each transmitter are $(\omega_1, \omega_2, \omega_3, \omega_4) = 2\pi c(1/\lambda_1, 1/\lambda_2, 1/\lambda_3, 1/\lambda_4)$. Each output of the star coupler distributor is inserted into the input port number $s = 1$ of the demultiplexers. The guided frequency corresponding to each demultiplexer output port l is adjusted to $\omega_{l1} = \omega_l$.

Since $\zeta_i(\omega)$ is a narrowband function around the central frequency ω_i and the dominant contribution of $\mathrm{A}_{j,l1}(\omega)$ is around the central frequency ω_l, the approximation $\mathrm{A}_{j,l1}(\omega)\zeta_i(\omega) \approx \delta_{il}\mathrm{A}_{j,l1}(\omega_l)\zeta_l(\omega)$ is applied to (14), and it is simplified to

$$|\psi\rangle_{\mathrm{S}}^{(3)} = \prod_{l=1}^{4}\left(\sum_{j=1}^{4}\mathrm{B}_{jl}\mathrm{A}_{j,l1}(\omega_l)\hat{a}_{j,l,\zeta_l}^{\dagger(3)}\right)|0\rangle^{(3)}. \tag{20}$$

Assume the first receiver performs quantum nondemolition projective measurement

$$\hat{P}_{11}(\omega_1) = |1_{11}(\omega_1)\rangle^{(3)\,(3)}\langle 1_{11}(\omega_1)|$$

where $|1_{11}(\omega_1)\rangle^{(3)} = \hat{a}_{1,1}^{\dagger(3)}(\omega_1)|0\rangle^{(3)}$. Hence, according to (16), (20) transforms to

$$\hat{P}_{11}(\omega_1))|\psi\rangle_{\mathrm{S}}^{(3)} = \bar{\gamma}_{1111}(\omega_1)|1_{11}(\omega_1)\rangle^{(3)} \times \prod_{l=2}^{4}\left(\sum_{j=1}^{4}\mathrm{B}_{jl}\mathrm{A}_{j,l1}(\omega_l)\hat{a}_{j,l,\zeta_l}^{\dagger(3)}\right)|0\rangle^{(3)} \tag{21}$$

where $\bar{\gamma}_{1111}(\omega_1) = \mathrm{B}_{11}\mathrm{A}_{1,11}(\omega_1)\zeta_1(\omega_1)$ and $\hat{a}_{j,l,\zeta_l}^{\dagger(3)} = \int d\omega\zeta_l(\omega)\hat{a}_{j,l}^{\dagger(3)}(\omega)$. As is clear from (21), whenever the first receiver's quantum detector PD_{11} fires, which is related to the signal with the wave-packet $\zeta_1(\omega)$, other receivers never see any detection in the corresponding photodetectors, i.e., $\mathrm{PD}_{j1}\forall j \in \{2, \ldots, L\}$. The success probability of the projective measurement leading to (21) is proportional to $|\bar{\gamma}_{1111}(\omega_1)|^2$. In the Lambdanet topology, using the balanced star coupler distribution factor $|\mathrm{B}_{ji}|^2 = 1/N$, the received signal decreases inversely proportional to the number of users N. This architecture-induced intensity loss is more significant than the photon loss in network devices, such as optical fibers and star couplers. Therefore, we ignored the device photon losses in the above mathematical modeling. However, for completeness, the lossy star coupler is presented in Appendix A, which should replace the ideal BS $\hat{\mathrm{B}}$ operator above to include the photon loss in the Lambdanet QWDM network. The main drawback of the Lambdanet topology in the quantum domain is that due to the no-cloning theorem, perfect quantum amplifiers cannot be implemented in the quantum communication channel to compensate for the architecture-induced intensity loss [44]. In Section IV, we investigate an alternative topology utilizing the WGR that can overcome the disadvantages of architecture-induced intensity loss.

IV. ROUTER-BASED QWDM NETWORK

As discussed in Section III, adding users decreases the intensity (or probability) of a received signal of the Lambdanet network. However, increasing the user number does not have a noticeable impact on the rate of a received signal of a WGR-based network. Since weak coherent or single-photon pulse sources are often used in secure quantum networks, such as QKD networks, designing network components with minimum loss is essential. Therefore, studying the network that employs a WGR instead of a star coupler is also helpful, which has been done in this section. In the WGR-based topology, comparing Fig. 3 with Fig. 1, a WGR ($\underline{\mathrm{S}}$) is substituted for a general wavelength distributor ($\underline{\mathrm{G}}$). A lossy AWG can play the role of the WGR in a real-world WGR-based communication topology. Unlike Lambdanet in WGR-based topology, transmitters can transmit a signal with a broad spectrum of wavelengths to communicate with different receivers simultaneously. The signal passing from the ith input port to the jth output port of WGR is specified by the narrowband signal with the central guided frequency ω_{ji}. The WGR-based communication system corresponding to N users can guide N possible narrowband signals with different central wavelengths $\lambda_1, \ldots, \lambda_N$ related to the guided frequency ω_{ji} of the router as $\omega_{ji} = \omega_{j-i+1\mathrm{mod}N} = 2\pi c/\lambda_{j-i+1\mathrm{mod}N}$. For instance, in the four-user WGR-based network depicted in Fig. 3, the narrowband signal with the central wavelength λ_2 included in a broadband signal transmitted by the QTx 2 ($i = 2$) appears at PD_{32} ($l = 2$) of QRx 3 ($j = 3$).

For comparing a WGR-based network with a star coupler-based network, it is convenient to examine a lossy WGR modeled by a unitary transfer matrix $\underline{\mathrm{S}}(\omega)$ studied in [45] and revisited in Appendix B. Appendix B demonstrates that a lossy WGR can be modeled by adding a frequency-dependent BS in each output port of a lossless WGR (for example, see Fig. 13). More precisely, a lossy $N \times N$ WGR is mathematically modeled by a unitary $2N \times 2N$ transfer matrix $\underline{\mathrm{S}}$ [see (106)]. In this modeling, N extra added input ports are in vacuum states, and N ancillary output ports are

IEEE Transactions on Quantum Engineering

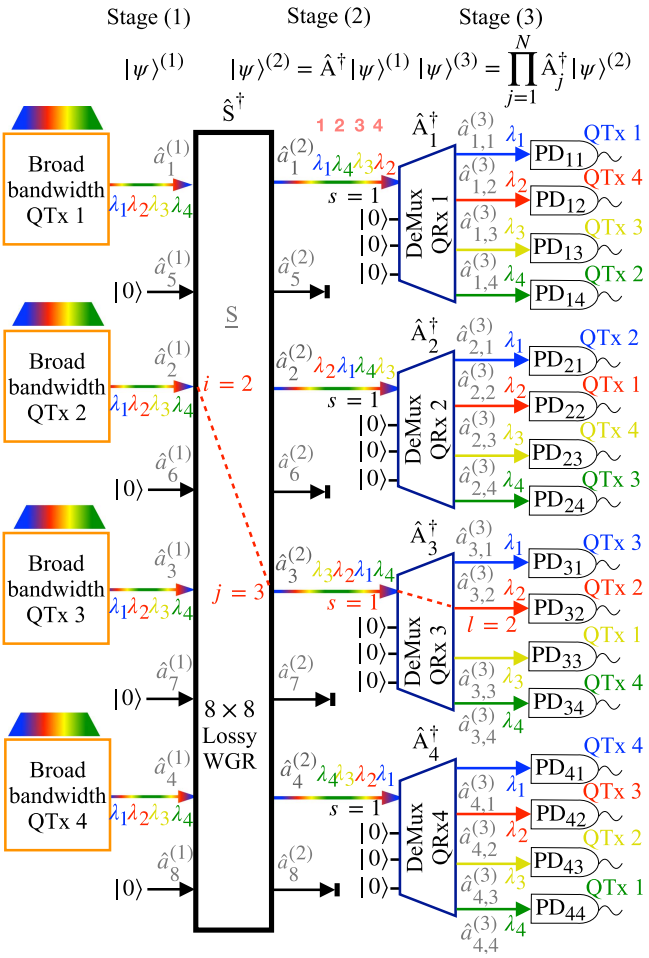

FIGURE 3. Schematic of quantum WDM network based on an 8 × 8 lossy WGR indicated by $\hat{\mathrm{S}}$.

blocked. For instance, Fig. 3 shows a 4 × 4 lossy WGR-based network modeled by a 8 × 8 unitary transfer matrix $\underline{\mathrm{S}}$.

In conclusion, in the WGR structure, operator $\underline{\mathrm{S}}$ plays the role of the generic distributor $\underline{\mathrm{G}}$ (see Section II and Fig. 1). Therefore, the input states $|\psi\rangle^{(1)}$ is evolved by $\hat{\mathrm{S}}^\dagger$ as $|\psi\rangle^{(1)} \xrightarrow{\hat{\mathrm{S}}^\dagger} |\psi\rangle^{(2)} = \hat{\mathrm{S}}^\dagger|\psi\rangle^{(1)}$. Subsequently, QRx (wavelength demultiplexers) separate the received signals according to their wavelength contents. Here, we assume demultiplexers are lossless AWGs because photon loss in receiver sites is ignorable compared to the transmission line. Thus, like the Lambdanet structure, the local unitary operator $\hat{\mathrm{A}}_j^\dagger$ evolves the state passing the jth QRx. Therefore, the global state at stage (3) becomes

$$|\psi\rangle^{(2)} \xrightarrow{\prod_{j=1}^{N}\hat{\mathrm{A}}_j^\dagger} |\psi\rangle^{(3)} = \prod_{j=1}^{N}\hat{\mathrm{A}}_j^\dagger|\psi\rangle^{(2)} = \prod_{j=1}^{N}\hat{\mathrm{A}}_j^\dagger\hat{\mathrm{S}}^\dagger|\psi\rangle^{(1)}.$$

In the upcoming subsections, the WGR-based QWDM communication system and network are studied when they are fed by coherent and single-photon signals as inputs, respectively.

A. COHERENT SIGNALS AS INPUTS

Assume all transmitters emit coherent states with broadband spectrums containing N narrowband signals with the central frequency $\omega \in \{\omega_1, \ldots, \omega_N\}$. According to (10), the spectral intensity at the output port jl becomes

$$\begin{aligned} I_{jl}(\omega_{ls}) &= {}^{(3)}_{\mathrm{C},jl}\langle\psi|\hat{a}^{\dagger(3)}_{j,l}(\omega_{ls})\hat{a}^{(3)}_{j,l}(\omega_{ls})|\psi\rangle^{(3)}_{\mathrm{C},jl} \\ &= \left|\sum_{i=1}^{2N}\alpha_i \mathrm{A}_{j,ls}(\omega_{ls})\mathrm{S}_{ji}(\omega_{ls})\zeta_i(\omega_{ls})\right|^2 \end{aligned} \tag{22}$$

where $\alpha_i = 0\ \forall i \in \{N+1, \ldots, 2N\}$ due to their related vacuum state inputs. Again, without loss of generality, we assume the received signal enters into port $s = 1$ of the QRx j, QRx j (see Fig. 3). In line with (96), (105), and (106), since the matrix element $\mathrm{S}_{ji}(\omega)$ for all $i, j \in \{1, \ldots, N\}$ has a nonzero value around the central frequency $\omega_{ji} = \omega_{j-i+1 \bmod N}$ with a narrow bandwidth $\Delta\omega_A$, it is approximated as $\mathrm{S}_{ji}(\omega_{l1}) \approx \mathrm{S}_{ji}(\omega_{l1})\delta_{l,(j-i+1)\bmod N}$ (neglecting the crosstalk effects). Thus, (22) is estimated as

$$\begin{aligned} I_{jl}(\omega_{l1}) &\approx |\alpha_{\bar{i}}\mathrm{A}_{j,l1}(\omega_{l1})\mathrm{S}_{j\bar{i}}(\omega_{l1})\zeta_{\bar{i}}(\omega_{l1})|^2 \\ &= |\alpha_{\bar{i}}\bar{\gamma}_{l1,j\bar{i}}(\omega_{l1})|^2 \end{aligned} \tag{23}$$

where $\bar{i} = (j - l + 1)\mathrm{mod}N$, $\omega_{j\bar{i}} = \omega_{l1} = \omega_l$, and (7) is used to derive the second line of (23). Moreover, the output state related to this receiver port according to (11) is approximated as

$$|\psi\rangle^{(3)}_{\mathrm{C},jl} \approx \hat{D}(\alpha_{\bar{i}}\bar{\gamma}_{l1,j\bar{i}})|0\rangle^{(3)}. \tag{24}$$

Equations (23) and (24) show that only the encoded information by the $\bar{i}$th transmitter reaches the output l of the jth receiver. Note that each variable $l \in \{1, \ldots, N\}$ is joined to distinguished transmitter $\bar{i} \in \{1, \ldots, N\}$. Therefore, if all transmitters' spectrum contains all WGR-guided frequencies, each receiver becomes independently connected to all the transmitters with a particular wavelength. The critical result of (23) is that although $|\mathrm{S}_{j\bar{i}}(\omega_{l1})|^2 < 1$ lowers the output spectral intensity, this degradation does not significantly change by increasing N compared to the frequency-independent term $|\mathrm{B}_{jl}|^2 \approx 1/N$ in (18) for the Lambdanet network. As a result, the lossy WGR network outperforms an ideal lossless Lambdanet network.

B. SINGLE-PHOTON SIGNALS AS INPUTS

Fig. 3 depicts a four-user communication system. Like the Lambdanet quantum network, one may assume each user holds a transmitter and a receiver device. The related unitary evolution of a 4 × 4 lossy WGR is modeled by a unitary operator $\hat{\mathrm{S}}^\dagger$ with eight inputs/outputs. We study two kinds of spectrally broadband sources of single photons, which senders may use. First, a broadband single-photon wave packet, and second, multiplexing a few narrowband single-photon sources with different central frequencies (see

Appendix B). In this subsection, a wave packet with a broadband spectrum is indicated by the symbol ζ, whereas a narrowband wave packet is shown by ξ.

1) BROADBAND SINGLE-PHOTON WAVE PACKET

Each transmitter transmits a broadband single-photon state as

$$|\psi_{\zeta_i}\rangle_{\mathrm{S}}^{(1)} = \hat{a}_{i,\zeta_i}^{\dagger(1)}|0\rangle^{(1)} = \int d\omega \zeta_i(\omega)\hat{a}_i^{\dagger(1)}(\omega)|0\rangle^{(1)} \tag{25}$$

where $\zeta_i(\omega)$ is a single-photon wave-packet profile. We assume this broadband single-photon state is in a superposition of all carrier frequencies $\{\omega_1, \omega_2, \omega_3, \omega_4\}$, where $\omega_n = 2\pi c/\lambda_n\, n \in \{1, \ldots, 4\}$.

Appendix A, studies a single-photon signal with the broadband spectrum $\zeta_i(\omega)$ passing through an ideal demultiplexer. It introduces new wave packets with narrowband spectrums $\xi_{i,n}(\omega)$ and carrier frequencies ω_n. Here, we analyze a system where all users utilize broadband single-photon sources. At the same time, the quantum wavelength distributor, the passive quantum router, is a lossy AWG (generally speaking, a lossy WGR).

Note that vacuum states feed auxiliary input ports of the lossy WGR model ($\underline{\mathrm{S}}$) $\forall i \in \{5, \ldots, 8\}$. Thus, the global state at the receiver site according to (14) becomes

$$|\psi\rangle_{\mathrm{S}}^{(3)} = \prod_{i=1}^{4}\left(\sum_{j=1}^{8}\sum_{l=1}^{4}\mathcal{N}_{l1ji}\hat{a}_{j,l,\gamma_{l1ji}}^{\dagger(3)}\right)|0\rangle^{(3)}. \tag{26}$$

Using (6) and (7), we expand the argument of (26) as follows:

$$\begin{aligned}\mathcal{N}_{l1ji}\hat{a}_{j,l,\gamma_{l1ji}}^{\dagger(3)} &= \int \mathrm{A}_{j,l1}(\omega)\mathrm{S}_{ji}(\omega)\zeta_i(\omega)\hat{a}_{j,l}^{\dagger(3)}(\omega)d\omega \\ &\approx \int \mathrm{A}_{j,l1}(\omega)\mathrm{S}_{ji}(\omega)\sum_{l'=1}^{4}c_{l'}\xi_{i,l'}(\omega)\hat{a}_{j,l}^{\dagger(3)}(\omega)d\omega \\ &\approx \mathrm{A}_{j,l1}(\omega_{l1})\mathrm{S}_{ji}(\omega_{l1})c_l\int \xi_{i,l}(\omega)\hat{a}_{j,l}^{\dagger(3)}(\omega)d\omega \\ &\approx \mathrm{A}_{j,l1}(\omega_{l1})\mathrm{S}_{ji}(\omega_{l1})c_l\hat{a}_{j,l,\xi_{i,l}}^{\dagger(3)}\end{aligned} \tag{27}$$

where we use two estimations as follows. First, due to the fact that both WGR and receivers have narrow bandwidth output signals around the guided frequencies $\omega_{l'} \in \{\omega_1, \ldots, \omega_4\}$, one can decompose the photon wave packet of the ith sender as $\zeta_i(\omega) = \sum_{l'=1}^{4} c_{l'}\xi_{i,l'}(\omega)$, where $\sum_{l'=1}^{4}|c_{l'}|^2 = 1$ and $\xi_{i,l'}(\omega)$ is a narrow bandwidth wave packet around the frequency $\omega_{l'}$ such that $\int \xi_{i,l'}^*(\omega)\xi_{i,l}(\omega)d\omega = \delta_{l,l'}$ (see Appendix A). Second, since the lth port of the jth receiver indicated by index jl guides a signal with the central frequency $\omega_{l1} = \omega_l$, in the two last lines of (27) we apply the estimation $\mathrm{A}_{j,l1}(\omega)\xi_{i,l'}(\omega) \approx \delta_{l,l'}\mathrm{A}_{j,l1}(\omega_{l1})\xi_{i,l}(\omega)$.

The signal at the output port jl of the demultiplexer $\mathrm{A}_{j,l1}(\omega)$ is dominant around the frequency ω_{l1} and the guided frequency of WGR, $\mathrm{S}_{ji}(\omega)$, from input port i to output port j is $\omega_{ji} = \omega_{j-i+1\mathrm{mod}4}$. Therefore, one can estimate $\mathrm{S}_{ji}(\omega_{l1}) \approx \mathrm{S}_{ji}(\omega_{l1})\delta_{l,\bar{l}}$ where $\bar{l} = (j-i+1)\mathrm{mod}4\ \forall i, j \in \{1, \ldots, 4\}$ and $\bar{l} = (j-4-i+1)\mathrm{mod}4\ \forall i \in \{1, \ldots, 4\}$ and $\forall j \in \{5, \ldots, 8\}$. Hence, (27) becomes

$$\begin{aligned}\mathcal{N}_{l1ji}\hat{a}_{j,l,\gamma_{l1ji}}^{\dagger(3)} &\approx \delta_{l,\bar{l}}\mathrm{A}_{j,l1}(\omega_{l1})\mathrm{S}_{ji}(\omega_{l1})c_l\hat{a}_{j,l,\xi_{i,l}}^{\dagger(3)} \\ &= \delta_{l,\bar{l}}C_{l1ji}\hat{a}_{j,l,\xi_{i,l}}^{\dagger(3)}\end{aligned} \tag{28}$$

where $C_{l1ji} = \mathrm{A}_{j,l1}(\omega_{l1})\mathrm{S}_{ji}(\omega_{l1})c_l$. As a result, (26) becomes

$$|\psi\rangle_{\mathrm{S}}^{(3)} = \prod_{i=1}^{4}\left(\sum_{j=1}^{4}C_{\bar{l}1ji}\hat{a}_{j,\bar{l},\xi_{i,\bar{l}}}^{\dagger(3)} + \sum_{j=5}^{8}C_{\bar{l}1ji}\hat{a}_{j,\bar{l},\xi_{i,\bar{l}}}^{\dagger(3)}\right)|0\rangle^{(3)}. \tag{29}$$

Note that receivers with index $j > 4$ are related to the auxiliary port of the lossy WGR distributor whose QRx $\hat{a}_{j,\bar{l},\xi_{i,\bar{l}}}^{\dagger(3)}$ are virtual, allowing us to use the generic formalism explained in Section II. Therefore, the second term on the right-hand side of (29) is related to the ancillary blocked receivers (see output ports of WGR in Fig. 3 indicated by $\hat{a}_j^{(2)}$ where $j \in \{5, \ldots, 8\}$), which degrades the system performance by consuming single photons. The presence of the creation mode $\hat{a}_{j,\bar{l},\xi_{i,\bar{l}}}^{\dagger(3)}$ in (29) restates that the ith transmitter is connected to the real (virtual) jth receiver with the specific frequency $\omega_{\bar{l}1} = \omega_{\bar{l}}$ where $\bar{l} = j - i + 1\mathrm{mod}4$ ($\bar{l} = j - 4 - i + 1\mathrm{mod}4$).

As a concrete example, given that the $\tilde{j}$th receiver performs the projective measurement by applying the local projective operator $\hat{P}_{\tilde{j}\tilde{l}}(\omega_{\tilde{l}}) = |1_{\tilde{j}\tilde{l}}(\omega_{\tilde{l}})\rangle^{(3)}\,{}^{(3)}\langle 1_{\tilde{j}\tilde{l}}(\omega_{\tilde{l}})|$ on (29), where index $\tilde{j}\tilde{l}$ indicates the $\tilde{l}$th output port of the $\tilde{j}$th receiver. Using the same procedure as in (28), for $j = \tilde{j}$ and $l = \tilde{l}$ (7) gives

$$\bar{\gamma}_{\bar{l}s\tilde{j}i'}(\omega_{\bar{l}1}) = \delta_{\bar{l},\tilde{l}}C_{\bar{l}s\tilde{j}i'}\xi_{i',\bar{l}}(\omega_{\bar{l}1}) = \delta_{i',\tilde{l}}C_{\bar{l}s\tilde{j}i'}\xi_{i',\tilde{l}}(\omega_{\bar{l}1}) \tag{30}$$

where, for example for receiver $\tilde{j} = 1$, $\bar{l} = (\tilde{j} - i' + 1)\mathrm{mod}4 = (2 - i')\mathrm{mod}4$, and equivalently, $\bar{i} = (2 - \tilde{l})\mathrm{mod}4$. We apply (30) on (16), assuming $\tilde{j} = 1$, and $s = 1$. Furthermore, according to (28), we substitute $\mathcal{N}_{l1ji}\hat{a}_{j,l,\gamma_{l1ji}}^{\dagger(3)}$ with $\delta_{l\bar{l}}C_{l1ji}\hat{a}_{j,l,\xi_{i,l}}^{\dagger(3)}$ in (16). As a result, the collapsed state of (29) after projective measurement $\hat{P}_{1\tilde{l}}(\omega_{\tilde{l}})$ becomes

$$\begin{aligned}\hat{P}_{1\tilde{l}}(\omega_{\tilde{l}})|\psi\rangle_{\mathrm{S}}^{(3)} &= \bar{\gamma}_{\bar{l}11\tilde{l}}(\omega_{\tilde{l}})|1_{1\tilde{l}}(\omega_{\tilde{l}})\rangle^{(3)} \\ &\quad\times\prod_{\substack{i=1\\ i\neq\tilde{i}}}^{4}\left(\sum_{j=1}^{8}C_{\bar{l}1ji}\hat{a}_{j,\bar{l},\xi_{i,\bar{l}}}^{\dagger(3)}\right)|0\rangle^{(3)}\end{aligned} \tag{31}$$

where $\bar{\gamma}_{\bar{l}11\tilde{l}}(\omega_{\tilde{l}}) = C_{\bar{l}11\tilde{l}}\xi_{\tilde{l},\bar{l}}(\omega_{\tilde{l}})$. Using approximation $\zeta_{\tilde{l}}(\omega_{\tilde{l}}) \approx c_{\tilde{l}}\xi_{\tilde{l},\tilde{l}}(\omega_{\tilde{l}})$, one can realize $\bar{\gamma}_{\bar{l}11\tilde{l}}(\omega_{\tilde{l}})$ has the same form as (7). Note that in (31), the index $\bar{l}$ is a variable that varies depending on the values of j and i. On the other hand, $\bar{i}$ and $\tilde{l}$ are fixed parameters and related to each other as $\bar{i} = 2 - \tilde{l}\mathrm{mod}4$. Equation (31) clarifies that the first receiver ($\tilde{j} = 1$) will receive the encoded information by the $\bar{i}$th transmitter ($\bar{i} = (2 - \tilde{l})\mathrm{mod}4$) on the carrier frequency $\omega_{\tilde{l}}$ with the probability proportional to $|\bar{\gamma}_{\bar{l}11\tilde{l}}(\omega_{\tilde{l}})|^2$. The photon

detection by the first receiver's quantum detector ($PD_{1\bar{i}}$) contains the information of transmitter QTx $\bar{i}$. After this detection, there is no chance of detection by other receivers' detectors, which can detect the broadband single-photon signal prepared by the $\bar{i}$th transmitter even in different frequencies $\omega_l \neq \omega_{\bar{l}}$.

2) MULTIPLEXED NARROWBAND SINGLE-PHOTON SOURCES

In this case, each user transmits four spectrally distinguished photons

$$|\psi\rangle_i^{(1)} = \prod_{n=1}^{4} \int d\omega \xi_{i,n}(\omega) \hat{a}_i^{\dagger(1)}(\omega)|0\rangle^{(1)} \tag{32}$$

where $\xi_{i,n}(\omega)$ is the nth narrowband spectrum prepared by the ith transmitter ($i \in \{1, \ldots, 4\}$) with the central frequency match to the guided frequency of WGR from its nth input toward its first output as $\omega_{1n} = \omega_n \, \forall n \in \{1, \ldots, 4\}$ such that $\int \xi_{i,n}^*(\omega)\xi_{i,n'}(\omega)d\omega \approx \delta_{n,n'}$. To better understand the meaning of (32), consider $\xi_{1,n}(\omega)$ as a wave packet of a photon with the horizontal polarization around the frequency ω_n transmitted by the first transmitter. In contrast, the wave-packet $\xi_{2,n'}(\omega)$ can correspond to a vertically polarized photon with central frequency $\omega_{n'}$ transmitted by the second transmitter. Generally speaking, the other transmitted photons from each transmitter may carry different polarizations. Note that additional degrees of freedom, such as time-bins or orbital angular momentums, could be information carriers to transmit encoded data from senders to receivers in a router-based QWDM network. The following shows how each encoded wave-packet $\xi_{i,n}(\omega)$ independently goes to a specific receiver. The practical usage of this topology in a QKD network will be discussed in Section VI-B.

Since the auxiliary input ports of $\underline{S}$ as a 8×8 unitary operator are in the vacuum state, the product sum on the input states in the following equation is up to $i = 4$ instead of $i = 8$. Therefore, in line with (32), the total state emitted by all transmitters becomes

$$\begin{aligned} |\psi\rangle^{(1)} &= \prod_{i=1}^{4} |\psi\rangle_i^{(1)} \\ &= \prod_{i=1}^{4}\prod_{n=1}^{4} \int d\omega \xi_{i,n}(\omega) \hat{a}_i^{\dagger(1)}(\omega)|0\rangle^{(1)} \\ &= \prod_{i=1}^{4}\prod_{n=1}^{4} \hat{a}_{i,\xi_{i,n}}^{\dagger(1)}|0\rangle^{(1)}. \end{aligned} \tag{33}$$

According to (14), the evolution of (33) to stage (3) becomes

$$|\psi\rangle_S^{(3)} = \prod_{i=1}^{4}\prod_{n=1}^{4} \left(\sum_{j=1}^{8}\sum_{l=1}^{4} \mathcal{N}_{l1\,ji,n} \hat{a}_{j,l,\gamma_{l1\,ji,n}}^{\dagger(3)} \right) |0\rangle^{(3)} \tag{34}$$

where $\mathcal{N}_{l1\,ji,n}$ and $\gamma_{l1\,ji,n}(\omega)$ are acquired by substituting $\xi_{i,n}(\omega)$ in place of $\zeta_i(\omega)$ in (3)–(5). Note that since each user emits a tensor product of single-photon states, all the related results in Section II require the above modification.

Because the central frequency of $\xi_{i,n}$ is fixed to $\omega_n = \omega_{1n}$ for all transmitters, the dominant part of the single-photon wave-packet $\gamma_{l1\,ji,n}(\omega)$, for the operator $\hat{a}_{j,l,\gamma_{l1\,ji,n}}^{\dagger(3)}$ in (34), occurs when $\omega \approx \omega_n = \omega_{l1} = \omega_{ji}$, leading to $n = l = (j - i + 1)\text{mod}4$. Remind that ω_{l1} is the guided frequency of the demultiplexer at receiver site from its first input to its lth output. Besides, ω_{ji} is the guided frequency of WGR from its ith input toward the jth output for $i, j \in \{1, 2, 3, 4\}$. Subsequently, similar to (27), $\forall\, i, j \in \{1, \ldots, 4\}$, the following approximation holds:

$$\begin{aligned} \mathcal{N}_{l1\,ji,n}\hat{a}_{j,l,\gamma_{l1\,ji,n}}^{\dagger(3)} &= \int \mathrm{A}_{j,l1}(\omega)\mathrm{S}_{ji}(\omega)\xi_{i,n}(\omega)\hat{a}_{j,l}^{\dagger(3)}(\omega)d\omega \\ &\approx \delta_{ln}\delta_{jj'}\mathrm{A}_{j,l1}(\omega_n)\mathrm{S}_{ji}(\omega_n)\hat{a}_{j,l,\xi_{i,n}}^{\dagger(3)} \end{aligned} \tag{35}$$

where $j' = (n + i - 1)\text{mod}4$. Furthermore, for all $i \in \{1, \ldots, 4\}$ and virtual ports $j \in \{5, \ldots, 8\}$

$$\begin{aligned} \mathcal{N}_{l1\,ji,n}\hat{a}_{j,l,\gamma_{l1\,ji,n}}^{\dagger(3)} &= \int \mathrm{A}_{j,l1}(\omega)\mathrm{S}_{ji}(\omega)\xi_{i,n}(\omega)\hat{a}_{j,l}^{\dagger(3)}(\omega)d\omega \\ &\approx \delta_{ln}\delta_{jj''}\mathrm{A}_{j,l1}(\omega_n)\mathrm{S}_{ji}(\omega_n)\hat{a}_{j,l,\xi_{i,n}}^{\dagger(3)} \end{aligned} \tag{36}$$

where $j'' = ((n + i - 1)\text{mod}4) + 4$. Substituting (35) and (36) to (34) gives rise to

$$\begin{aligned} |\psi\rangle_S^{(3)} = \prod_{i=1}^{4}\prod_{n=1}^{4} &(\mathrm{A}_{j',n1}(\omega_n)\mathrm{S}_{j'i}(\omega_n)\hat{a}_{j',n,\xi_{i,n}}^{\dagger(3)} \\ &+ \mathrm{A}_{j'',n1}(\omega_n)\mathrm{S}_{j''i}(\omega_n)\hat{a}_{j'',n,\xi_{i,n}}^{\dagger(3)})|0\rangle^{(3)}. \end{aligned} \tag{37}$$

According to (37), at the nth demultiplexer's output port of receiver $j' = (n + i - 1) \bmod 4$, the distinguished signal of sender i with the central frequency ω_n (indicated by the creation operator $\hat{a}_{j',n,\xi_{i,n}}^{\dagger(3)}$) is delivered. Hence, all the transmitters are simultaneously connected to all the receivers and function independently. Note that the correlation in (37) is due to the introduced BSs as a loss model. For an ideal, lossless WGR ($\mathrm{S}_{j''i}(\omega) = 0$ and $|\mathrm{A}_{j',n1}(\omega_n)| = |\mathrm{S}_{j'i}(\omega_n)| = 1$), the final state at stage (3) becomes separable as follows:

$$|\psi\rangle_S^{(3)} = \prod_{i=1}^{4}\prod_{n=1}^{4} \mathrm{A}_{j',n1}(\omega_n)\mathrm{S}_{j'i}(\omega_n)\hat{a}_{j',n,\xi_{i,n}}^{\dagger(3)}. \tag{38}$$

V. FIBER-TO-THE-QUANTUM NODE QWDM NETWORK

For the last but not least example of a conventional network in the quantum domain, we study the quantum version of one of the most used WDM local access networks, which utilizes the fiber optic capacity, i.e., FTTH. This topology connects local users to a remote node via separate fiber optics. A remote node is a wavelength multiplexer/demultiplexer connected to the central office via a single optical fiber. The central office hub demultiplexes the received signals and multiplexes the transmitting signals to the remote node destination. The number of receivers and transmitters in the

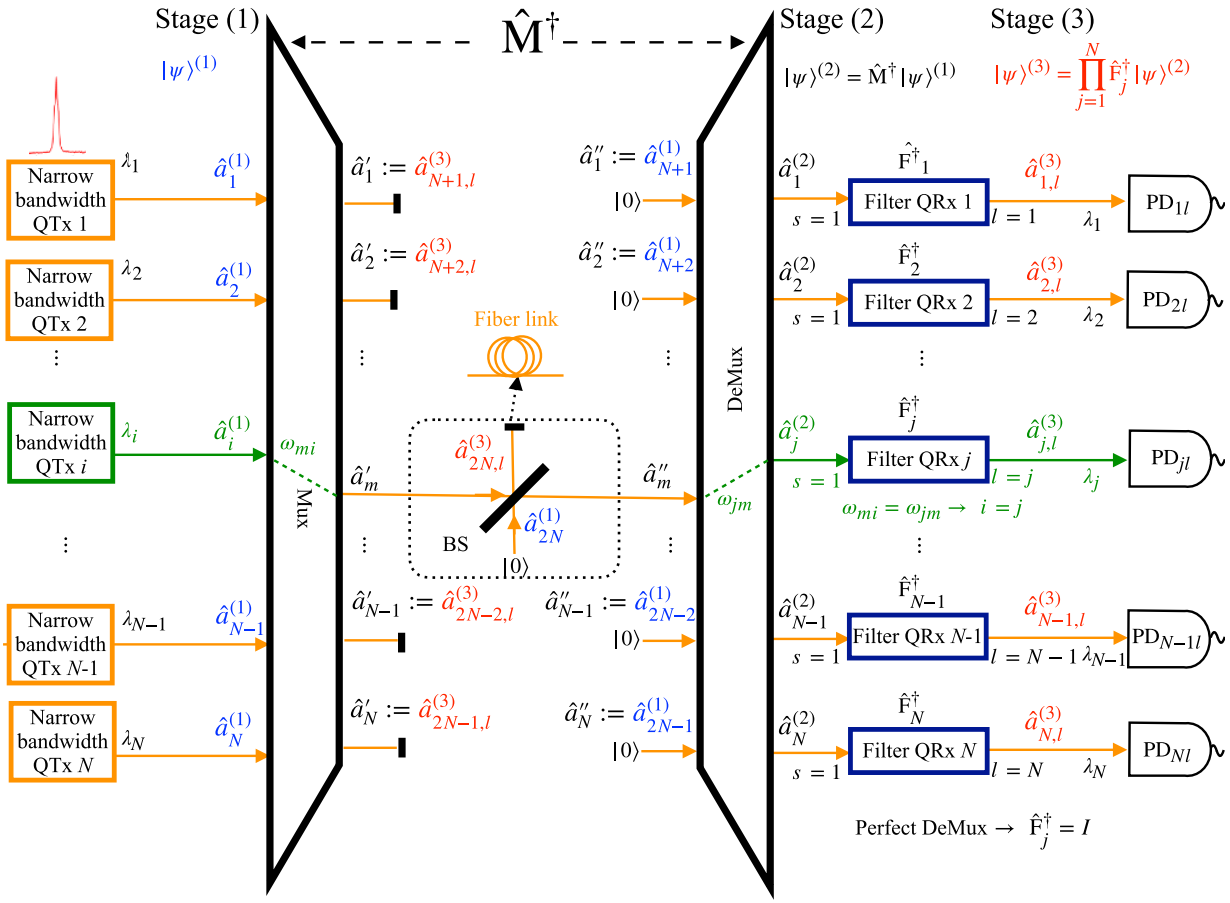

FIGURE 4. FTTQ. The fiber link is modeled by a BS. Mux and DeMux are abbreviations of wavelength division multiplexer and demultiplexer.

hub equals users' sites. Consequently, multiplexing and demultiplexing of signals form a passive photonic loop. Here, we mathematically model this topology, assuming all the receivers are in the users' sites while all the transmitters are in the central office. This is similar to the long-haul point-to-point WDM networks, as shown in Fig. 4.

Fig. 4 illustrates a quantum mathematical model for conventional passive photopic loop and long-haul point-to-point WDM networks, which we name FTTQ node (quantum transmitter and receiver) [13], [15]. This figure shows that an optical fiber link connects N transmitters and N receivers via wavelength multiplexing and demultiplexing the signals. The quantum operator $\hat{\mathrm{M}}^{\dagger}$ models the combination of multiplexer-fiber-demultiplexer, which plays the role of wavelength distributors indicated in Fig. 1, i.e., $\hat{\mathrm{G}}^{\dagger} = \hat{\mathrm{M}}^{\dagger}$. Although in the classical world, multiplexers and demultiplexers are $N \times 1$ and $1 \times N$ devices, in quantum mechanics, they are modeled by $N \times N$ transfer matrix, where multiplexers have $N-1$ auxiliary blocked output ports, and demultiplexers have $N-1$ auxiliary vacuum input ports. Furthermore, a BS models a lossy optical fiber link with a transmission coefficient that equals the fiber transmittance. We label the BS's extra input and output ports of the fiber link as the $2N$th input and output ports of the operator $\hat{\mathrm{M}}^{\dagger}$ (see Fig. 4). Suppose all transmitters use narrow-bandwidth sources in the FTTQ topology, and receivers utilize narrow bandpass filters. For simplicity, it is also assumed that the demultiplexer's output bandwidth is much less than the filter's bandwidth; therefore, one can estimate the quantum unitary transforms of the filters as identity operators. Thereby, as shown in Fig. 4, the narrowband signals emitted by the QTx are first combined by the wavelength multiplexer (Mux) to the output mode indicated by $\hat{a}'_m$. Then, after passing through the virtual BS as a model of a lossy optical fiber link, the N combined signals are separated by the wavelength demultiplexer (DeMux) to N spatially different ports, reaching different receivers.

Wavelength multiplexers and demultiplexers used in FTTQ networks can be implemented by a $N \times N$ arrayed waveguide grating (AWG) whose quantum model $\hat{\mathrm{A}}$ is briefly explained in Appendix B according to the materials of [45] and [46]. It may be wise to think of a demultiplexer evolution operator as an inverse (transpose conjugate) of a multiplexer evolution operator. By proper rearrangement of input labels, the AWG as a Mux or a Demux treats symmetrically, i.e., $\hat{\mathrm{A}}^{\dagger} = \hat{\mathrm{A}}$. Thus, the unitary operators corresponding

IEEE Transactions on Quantum Engineering

to the evolution of signals through the wavelength multiplexer and the wavelength demultiplexer are described by the same quantum operator $\hat{\mathrm{A}}$. This means that the guided frequency from the ith input toward the jth output of the AWG equals the jth input toward the ith output, i.e., $\omega_{ji} = \omega_{ij}$ [15]. As illustrated in Fig. 4 and according to (95b), the Mux transforms the input mode $(\hat{a}_i^{(1)}(\omega))$ to output mode $(\hat{a}'_j(\omega))$ as

$$\hat{a}_i^{(1)}(\omega) = \sum_{j=1}^{N} \mathrm{A}^*_{ji}(\omega)\hat{a}'_j(\omega) \tag{39}$$

and the input mode $(\hat{a}''_i(\omega))$-output mode $(\hat{a}_j^{(2)}(\omega))$ relation for Demux is given by

$$\hat{a}''_i(\omega) = \sum_{j=1}^{N} \mathrm{A}^*_{ji}(\omega)\hat{a}_j^{(2)}(\omega). \tag{40}$$

The BS as a 2×2 unbalanced star coupler (see Appendix A) leads to the connection between Mux output mode $(\hat{a}'_m(\omega))$ and DeMux input mode $(\hat{a}''_m(\omega))$ as

$$\hat{a}'_m(\omega) = \mathrm{B}_{11}^{*f}\hat{a}_{2N,l}^{(3)}(\omega) + \mathrm{B}_{21}^{*f}\hat{a}''_m(\omega) \tag{41}$$

where superscript f presented on the BS coefficients (B_{11}^{*f} and B_{21}^{*f}) signifies that the BS is an optical fiber link model. Assume that $\hat{\mathrm{F}}_j = I$; therefore, the mode in stage (2) equals stage (3), and the received modes in stage (3) are written as $\hat{a}_{j,l}^{(3)} = \hat{a}_j^{(2)}$, where the quantum model of the filter can be viewed as a virtual $N \times N$ AWG in which only one of its output ports denoted by l is used, and others are blocked. The used output port l related to the jth receiver of this virtual AWG model is fixed to the port, which allows passing wavelength λ_j. For instance, it is assumed in the virtual AWG model of filters depicted in Fig. 4 that if the AWG input port is fixed to $s = 1$, a narrowband signal with the central wavelength λ_j exits from the output port $l = j$. Since we assume all the receivers have identical QRx, in Fig. 4, the output port of the jth QRx is indicated by $l = j$. For the auxiliary receivers, the index l is a parameter to help the model provide consistent indexing with the most general case. Note that since the presented network at most supports N different frequencies if the auxiliary blocked output ports from $N+1$ to $2N$ are equipped with demultiplexers, their output indexes would be $l \in \{1, \ldots, N\}$. Let us highlight that, in this section, in FTTQ structure for simplicity, we have assumed that the guided frequency for the filters is $\omega_{l1} = \omega_l = 2\pi c/\lambda_l$, while for Mux–DeMux structure $\omega_{mi} = \omega_{jm} = \omega_i = 2\pi c/\lambda_i$ for $i = j$.

Adapting the general topology indexing given in (2), the auxiliary vacuum input ports of DeMux are renamed as

$$\hat{a}_{N+i}^{(1)} = \hat{a}''_i \text{ for } i \in \{1, \ldots, m-1\}$$
$$\hat{a}_{N+i-1}^{(1)} = \hat{a}''_i \text{ for } i \in \{m+1, \ldots, N\}.$$

Moreover, the auxiliary blocked output ports of Mux are relabeled as

$$\hat{a}_{N+i,l}^{(3)} = \hat{a}'_i \text{ for } i \in \{1, \ldots, m-1\}$$
$$\hat{a}_{N+i-1,l}^{(3)} = \hat{a}'_i \text{ for } i \in \{m+1, \ldots, N\}.$$

These ancillary inputs and outputs, along with the unused BS input port $\hat{a}_{2N}^{(1)}$ and the blocked output port $\hat{a}_{2N,l}^{(3)}$, aggregate to model an $N \times N$ Mux–Fiber–DeMux system with a $2N \times 2N$ quantum operator, denoted by $\hat{\mathrm{M}}^\dagger$. As a result, the overall input–output mode relation for this compound system is written as

$$\hat{a}_i^{\dagger(1)}(\omega) = \sum_{j=1}^{2N} \mathrm{M}_{ji}(\omega)\hat{a}_{j,l}^{\dagger(3)}(\omega) := \hat{\mathrm{M}}^\dagger \hat{a}_i^{\dagger(1)}(\omega)\hat{\mathrm{M}}. \tag{42}$$

Accordingly, the evolution of a general input state (1) to stage (3) becomes

$$|\psi\rangle^{(3)} = \hat{\mathrm{M}}^\dagger |\psi\rangle^{(1)} = \prod_{i=1}^{2N} f_i \left(\int d\omega \zeta_i(\omega) \{\hat{\mathrm{M}}^\dagger \hat{a}_i^{\dagger(1)}(\omega)\hat{\mathrm{M}}\} \right) |0\rangle^{(3)}. \tag{43}$$

Using (39)–(43) accompanied with the above mode renaming, the global state in stage (3) becomes

$$\begin{aligned} |\psi\rangle^{(3)} = \prod_{i=1}^{N} f_i \Bigg(\int d\omega \zeta_i(\omega) \Bigg\{ & \sum_{j=1}^{N} \mathrm{A}_{mi}(\omega)\mathrm{B}_{21}^f \mathrm{A}_{jm}(\omega)\hat{a}_{j,l}^{\dagger(3)}(\omega) \\ & + \sum_{j=N+1}^{N+m-1} \mathrm{A}_{j-N,i}(\omega)\hat{a}_{j,l}^{\dagger(3)}(\omega) \\ & + \sum_{j=N+m}^{2N-1} \mathrm{A}_{j-N+1,i}(\omega)\hat{a}_{j,l}^{\dagger(3)}(\omega) \\ & + \mathrm{A}_{mi}(\omega)\mathrm{B}_{11}^f \hat{a}_{2N,l}^{\dagger(3)}(\omega) \Bigg\} \Bigg) |0\rangle^{(3)} \end{aligned} \tag{44}$$

where for $i \in \{N+1, \ldots, 2N\}$, $f_i(\hat{a}_{\zeta_i}^\dagger) = 1$, and the following substitution in (44) [or equivalently in (43)] is used:

$$\begin{aligned} & \mathrm{G}_{ji}(\omega) = \mathrm{M}_{ji}(\omega) = \mathrm{A}_{mi}(\omega)\mathrm{B}_{21}^f \mathrm{A}_{jm}(\omega) \quad j \in \{1, \ldots, N\} \\ & \mathrm{G}_{ji}(\omega) = \mathrm{M}_{ji}(\omega) = \mathrm{A}_{j-N,i}(\omega) \quad j \in \{N+1, \ldots, N+m-1\} \\ & \mathrm{G}_{ji}(\omega) = \mathrm{M}_{ji}(\omega) = \mathrm{A}_{j-N+1,i}(\omega) \quad j \in \{N+m, \ldots, 2N-1\} \\ & \mathrm{G}_{ji}(\omega) = \mathrm{M}_{ji}(\omega) = \mathrm{A}_{mi}(\omega)\mathrm{B}_{11}^f \quad j = 2N. \end{aligned} \tag{45}$$

Note that the filter passes frequency ω_{jm} and since in an ideal FTTQ system, only frequency band ω_{jm} reaches the filter $\hat{\mathrm{F}}_j$; therefore, its operation is approximated with the identity operator from its input $s = 1$ to output $l = j$, i.e., $\mathrm{QRx}_j = \hat{\mathrm{F}}_j = I$. The Mux's and DeMux's input and output ports are arranged in such a way that $\omega_{mi} = \omega_{jm}$ provided $i = j$ (For example, by exchanging input port numbers 2 with 4 of a 4×4 AWG depicted in Fig. 11.). Thus, there

is a one-to-one relation between transmitted and received frequencies (see Fig. 4), i.e., the first transmitter is linked to the first receiver, the second transmitter is linked to the second receiver, and so on.

A. COHERENT SIGNALS AS INPUTS

In this part, we concentrate on the FTTQ communication system when all the transmitters prepare coherent state signals [given in (8)] for transporting information. Consider the approximation

$$|\mathrm{A}_{ji}(\omega)|^2 \approx \begin{cases} 1, & |\omega-\omega_{ji}| \le \Delta\omega_{\mathrm{A}}/2 \\ 0, & \text{otherwise} \end{cases} \tag{46}$$

for the wavelength Mux and DeMux. Using (10), and the estimation $\mathrm{A}_{mi}(\omega_{jm}) \approx \delta_{ij}\mathrm{A}_{mj}(\omega_{jm})$ concluded from (46) (neglecting the crosstalk), the spectral intensity at the jth receiver' site ($j \le N$) becomes

$$\begin{aligned} I_{jj}(\omega_{jm}) &= {}^{(3)}_{\mathrm{C},jj}\langle\psi|\hat{a}^{\dagger(3)}_{j,j}(\omega_{jm})\hat{a}^{(3)}_{j,j}(\omega_{jm})|\psi\rangle^{(3)}_{\mathrm{C},jj} \\ &\approx \left|\sum_{i=1}^{N}\alpha_i\mathrm{A}_{mi}(\omega_{jm})\mathrm{B}^{f}_{21}\mathrm{A}_{jm}(\omega_{jm})\zeta_i(\omega_{jm})\right|^2 \\ &\approx |\alpha_j\mathrm{A}_{mj}(\omega_{jm})\mathrm{B}^{f}_{21}\mathrm{A}_{jm}(\omega_{jm})\zeta_j(\omega_{jm})|^2 \\ &\approx |\alpha_j|^2|\mathrm{B}^{f}_{21}|^2|\zeta_j(\omega_{mj})|^2. \end{aligned} \tag{47}$$

Equation (47) indicates that the ith transmitter is linked to the jth receiver providing $i=j$. Note that the AWG output port number as a model for the filter is assumed to be fixed to the receiver number, i.e., $l=j$. Equation (47) shows that the intensity $I_{jj}(\omega_{jm})$ is proportional to the frequency amplitude $|\zeta_j(\omega_{jm})|^2$ of the jth transmitter, and its mean photon number $|\alpha_j|^2$. The fiber transmittance coefficient can be approximated as $|\mathrm{B}^{f}_{21}|^2 = 10^{-\bar{\alpha}\mathscr{L}/10}$, where $\bar{\alpha}=0.2$ dB/km and $\mathscr{L}$ are the fiber loss per kilometer and the length between Mux and DeMux, respectively [15]. Using the Kelley–Kleiner formula [42], the probability of photon counting in the single-photon detector of the jth receiver is proportional to $[1-\exp(-\eta I_{jj}(\omega_{jm})\Delta\omega_{\mathrm{A}})]$, where η is the detector's efficiency, and $\Delta\omega_{\mathrm{A}}$ is the channel bandwidth of the AWG. If transmitters emit weak coherent pulses as inputs, i.e., $|\alpha_i|^2 \ll 1$, the probability that a single-photon detector click is commensurate with $I_{jj}(\omega_{jm})$.

Note that the ancillary blocked output port of the BS would receive the following intensity:

$$\begin{aligned} I_{2N,l}(\omega_{lm}) &\approx \left|\sum_{i=1}^{N}\alpha_i\mathrm{A}_{mi}(\omega_{lm})\mathrm{B}^{f}_{11}\zeta_i(\omega_{lm})\right|^2 \\ &\approx |\alpha_l\mathrm{A}_{ml}(\omega_{lm})\mathrm{B}^{f}_{11}\zeta_l(\omega_{lm})|^2. \end{aligned} \tag{48}$$

By employing a wavelength demultiplexer (where its input index is m, and its output indexes are indicated by different $l \in \{1,\ldots,N\}$) located at the BS's site (at the optical fiber link), an eavesdropper can access to the signal of the lth transmitter $l \in \{1,\ldots,N\}$, meaning the transmitters' information leaks to this virtual port. This is reminiscent of BS attacks in QKD protocols.

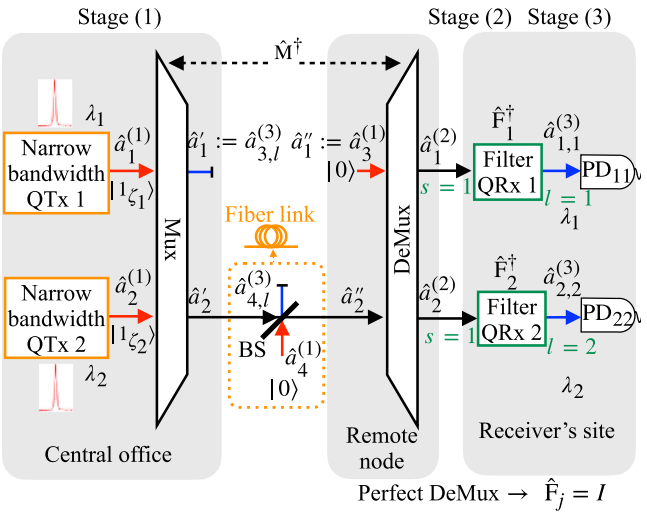

FIGURE 5. 4 × 4 quantum operator model for two-user (receiver) one-way FTTQ topology. Red and blue arrows indicate input and output signals, respectively.

B. SINGLE-PHOTON SIGNALS AS INPUTS

This section studies an FTTQ communication system comprising two transmitters, two receivers, and transmitters equipped with single-photon sources as given in (13). Considering the ancillary ports, such a system is expressible by a 4×4 distributer $\hat{\mathrm{M}}^{\dagger}$ as depicted in Fig. 5. In a long-haul fiber link topology, transmitters and receivers will be in different geographical locations. However, in a passive photonic loop topology, one transmitter and one receiver are placed in the location of each user (see [13, Fig. 1]).

Like Fig. 4, we assume the QRx are the ideal filters, taking signals from the input index $s=1$ and transporting the signals from the receivers' output port $l=j$ for $j\in\{1,2\}$. Since the QRx $j\in\{3,4\}$ are not equipped to any QRx's devices, the index l for these receivers is a dummy index and does not need sum over them in (14). Moreover, because input ports $i=3$ and $i=4$ are fed by vacuum states, the sum-product on i in (1) remains only on $i\in\{1,2\}$. Therefore, using (14), the state at stage (3) becomes

$$\begin{aligned} |\psi\rangle^{(3)}_{\mathrm{S}} = &\Big(\mathscr{N}_{1111}\hat{a}^{\dagger(3)}_{1,1,\gamma_{1111}} + \mathscr{N}_{2121}\hat{a}^{\dagger(3)}_{2,2,\gamma_{2121}} \\ &+ \mathscr{N}_{l131}\hat{a}^{\dagger(3)}_{3,l,\gamma_{l131}} + \mathscr{N}_{l141}\hat{a}^{\dagger(3)}_{4,l,\gamma_{l141}}\Big) \\ &\times\Big(\mathscr{N}_{1112}\hat{a}^{\dagger(3)}_{1,1,\gamma_{1112}} + \mathscr{N}_{2122}\hat{a}^{\dagger(3)}_{2,2,\gamma_{2122}} \\ &+ \mathscr{N}_{l132}\hat{a}^{\dagger(3)}_{3,l,\gamma_{l132}} + \mathscr{N}_{l142}\hat{a}^{\dagger(3)}_{4,l,\gamma_{l142}}\Big)|0\rangle^{(3)} \end{aligned} \tag{49}$$

IEEE Transactions on Quantum Engineering

where $\mathcal{N}_{lsji}$ and γ_{lsji} are obtained by (3), and (5). In addition, according to (7) and (45), the unnormalized modified wave packets contributing in (49) $\forall i,\ j \in \{1, 2\}$ are

$$\begin{aligned}
\bar{\gamma}_{j1ji}(\omega) &= \mathrm{M}_{ji}(\omega)\zeta_i(\omega) = \mathrm{A}_{mi}(\omega)\mathrm{B}^{f}_{21}\mathrm{A}_{jm}(\omega)\zeta_i(\omega) \\
\bar{\gamma}_{l13i}(\omega) &= \mathrm{M}_{3i}(\omega)\zeta_i(\omega) = \mathrm{A}_{1i}(\omega)\zeta_i(\omega) \\
\bar{\gamma}_{l14i}(\omega) &= \mathrm{M}_{4i}(\omega)\zeta_i(\omega) = \mathrm{A}_{mi}(\omega)\mathrm{B}^{f}_{11}\zeta_i(\omega). \qquad (50)
\end{aligned}$$

In (50), $\mathrm{A}_{jm}(\omega)$ and $\mathrm{A}_{mi}(\omega)$ have nonzero values around the central frequencies ω_j and ω_i, respectively. Hence, whenever $j \neq i$ the $\bar{\gamma}_{j1ji}(\omega)$ becomes zero. Furthermore, $\mathrm{A}_{1i}(\omega)$ is null around the central frequency of $\zeta_i(\omega)$, i.e., ω_i. Therefore, (49) is simplified to

$$\begin{aligned}
|\psi\rangle^{(3)}_{\mathrm{S}} &= \left(\mathcal{N}_{1111}\hat{a}^{\dagger(3)}_{1,1,\gamma_{1111}} + \mathcal{N}_{l141}\hat{a}^{\dagger(3)}_{4,l,\gamma_{l141}}\right) \\
&\quad \times \left(\mathcal{N}_{2122}\hat{a}^{\dagger(3)}_{2,2,\gamma_{2122}} + \mathcal{N}_{l142}\hat{a}^{\dagger(3)}_{4,l,\gamma_{l142}}\right)|0\rangle^{(3)} \\
&= \mathcal{N}_{1111}\mathcal{N}_{2122}|1_{\gamma_{1111}}1_{\gamma_{2122}}0_{\gamma_{l141}}0_{\gamma_{l142}}\rangle \\
&\quad + \mathcal{N}_{1111}\mathcal{N}_{l142}|1_{\gamma_{1111}}0_{\gamma_{2122}}0_{\gamma_{l141}}1_{\gamma_{l142}}\rangle \\
&\quad + \mathcal{N}_{2122}\mathcal{N}_{l141}|0_{\gamma_{1111}}1_{\gamma_{2122}}1_{\gamma_{l141}}0_{\gamma_{l142}}\rangle \\
&\quad + \mathcal{N}_{l141}\mathcal{N}_{l142}|0_{\gamma_{1111}}0_{\gamma_{2122}}1_{\gamma_{l141}}1_{\gamma_{l142}}\rangle. \qquad (51)
\end{aligned}$$

Equation (51) shows the entangled state between real $(\hat{a}^{\dagger(3)}_{1,1,\gamma_{1111}}|0\rangle = |1_{\gamma_{1111}}\rangle,\ \hat{a}^{\dagger(3)}_{2,2,\gamma_{2122}}|0\rangle = |1_{\gamma_{2122}}\rangle)$ and auxiliary $(\hat{a}^{\dagger(3)}_{4,l,\gamma_{l141}}|0\rangle = |1_{\gamma_{l141}}\rangle,\ \hat{a}^{\dagger(3)}_{4,l,\gamma_{l142}}|0\rangle = |1_{\gamma_{l142}}\rangle)$ output states at stage (3). Provided the first receiver (or user indicated by $\hat{a}^{(3)}_{1,1}$ in Fig. 5) receives the single photon in the state $|1_{11}(\omega_1)\rangle$, the collapsed state of $|\psi\rangle^{(3)}_{\mathrm{S}}$ after the projective measurement $\hat{P}_{11}(\omega_1) = |1_{11}(\omega_1)\rangle\langle 1_{11}(\omega_1)|$ becomes

$$\begin{aligned}
\hat{P}_{11}(\omega_1)|\psi\rangle^{(3)}_{\mathrm{S}} &= \bar{\gamma}_{1111}(\omega_1)|1_{11}(\omega_1)\rangle \\
&\quad \times \{\mathcal{N}_{2122}|1_{\gamma_{2122}}0_{\gamma_{l141}}0_{\gamma_{l142}}\rangle \\
&\quad + \mathcal{N}_{l142}|0_{\gamma_{2122}}0_{\gamma_{l141}}1_{\gamma_{l142}}\rangle\} \qquad (52)
\end{aligned}$$

with the detection probability proportional to $|\bar{\gamma}_{1111}(\omega_1)|^2$ [see (16)]. As seen in (52), the second receiver (or user indicated by $\hat{a}^{(3)}_{2,2}$ in Fig. 5) does not have access to the encoded information on the single-photon state $|1_{11}(\omega_1)\rangle$ received by the first receiver. As a result, the central office can communicate with both receivers independently and securely. The leakage of information dedicated to the first receiver toward the second receiver due to the crosstalk is characterized by the amount of $\bar{\gamma}_{2121}(\omega_1)$ [see (50) and when in nonideal AWG, $\mathrm{A}_{22}(\omega_1) \neq 0$]. The crosstalk can be eliminated by increasing user frequency channel spacing. Furthermore, assuming transmitters utilize ideal single-photon sources, the BS output port related to $\hat{a}^{(3)}_{4,l}$ gives rise to the signal loss in the system. Whenever any detection occurs in the output port related to the mode $\hat{a}^{(3)}_{4,l}$, the detector of the receiver who was supposed to receive that signal never clicks apart from the dark count of its nonideal single-photon detector.

Using nonideal single-photon sources or weak coherent pulses leads to security issues in cryptography applications.

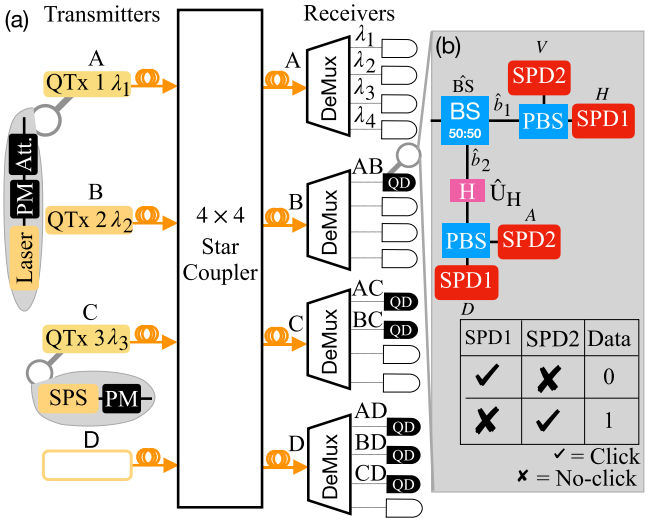

FIGURE 6. Schematic configuration of polarization encoded BB84-QKD based quantum WDM network using the star coupler among four users, A: Alice, B: Bob, C: Charlie, and D: David. QT: quantum transmitter, BS: beam splitter, PBS: polarization beam splitter, SPD: single-photon detector, H: half wave-plate, DeMux: demultiplexer, PM: polarization modulator, Att.: attenuator, SPS: single-photon source.

Assuming the central office is trustful, the information of users via the BS output port related to $\hat{a}^{(3)}_{4,l}$ can leak to an illegitimate eavesdropper. The BS model for the fiber link is the reminiscence of the well-known BS attack utilized by the eavesdropper in secure quantum communication protocols, such as QKDs [47]. This leaked information quantified by $\bar{\gamma}_{l141}(\omega_1)$ and $\bar{\gamma}_{l142}(\omega_2)$ must be excluded in the postprocessing procedure (privacy amplification [48]). Hence, the secure key rate of QKD protocols is limited.

VI. APPLICATIONS OF QWDM COMMUNICATION SYSTEMS IN QKD NETWORKS

This section studies the BB84 protocol as a well-known prepare and measure-based discrete-variable QKD protocol in the Lambdanet and WGR-based QWDM network topologies [39]. For the sake of simplicity, a four-user QKD network is analyzed. The generalization of this QKD-based network for N users is straightforward.

In a point-to-point polarization-encoded BB84 QKD protocol (a two-user network), a transmitter, Alice, randomly encodes classical bit into the polarization of input signals choosing either a rectilinear basis [horizontal (H) and vertical (V)] or a diagonal basis [diagonal (D) and an antidiagonal (A)]. The information carrier can be either single-photon or weak coherent pulses. The receiver, Bob, randomly chooses the rectilinear or diagonal measurement bases for polarization measurement. He decodes the information encoded in the polarization of signals based on the predetermined coding model. For example, horizontal or diagonal polarization signals are dedicated to bit 0. In contrast, vertical or antidiagonal polarized signals are related to bit 1.

Fig. 6(b) depicts a scheme for random basis selection for polarization measurement. The transmitted (reflected) output of the 50:50 BS corresponds to measurement on the rectilinear (diagonal) basis. A half-wave plate (H) transforms diagonal (antidiagonal) polarization to horizontal (vertical) one. Therefore, with the use of a polarization BS (PBS), which transmits (reflects) horizontal (vertical) polarization, and H wave plates, it is possible also to separate diagonal and antidiagonal polarizations. If an electro-optical polarization switch replaces the BS, the number of SPD used in a quantum detection setup (QD) is halved [49]. A correlation can only be drawn between Alice's and Bob's bits related to the same prepared and measured bases. Therefore, a sifting process is required to remove uncorrelated bits related to incompatible bases [39]. This section is processed as follows. First, Section VI-A studies the polarization-encoded BB84 QKD network in the Lambdanet topology based on the 4×4 star coupler. Second, the QKD network based on the WGR is analyzed in Section VI-B. Finally, in Section VI-C, a comparison between these two QKD networks is made with the help of existing experimental parameters.

A. LAMBDANET-BASED QKD NETWORK

Fig. 6 shows a 4×4 quantum WDM network between four users, Alice (A), Bob (B), Charlie (C), and David (D). Each user can have both transmitter and receiver setups. Nevertheless, for this fully connected QKD network, only three users, Alice, Bob, and Charlie, need QTx. Furthermore, only Bob's, Charlie's, and David's sites must be equipped with the measurement setups, i.e., QD (see the inset at the right-hand side of Fig. 6). Since David does not send any quantum signal in this scheme, the four-user QKD-based WDM network runs by only three wavelengths. Fig. 6 assumes that the QTx consists of a quasi-monochromatic single-photon source or an attenuated narrowband laser source accompanied by a polarization-modulating system. The signal transmitted from Alice's site passes through the detection parts related to Bob (AB), Charlie (AC), and David (AD). Thus, Alice can share the distinguished quantum keys with Bob, Charlie, and David. It is worth mentioning that provided the transmitted signal from Alice's site is an ideal single photon, Bob, Charlie, and David will not receive a similar signal simultaneously. So, any pair achieves a different and independent secret key. When the weak coherent source is used, the network-extended decoy-state scheme of the BB84 protocol compensates for the security issue that arises from the multiphoton states [50]. Since utilizing coherent sources is, in practice, very common, all transmitters are assumed to emit weak coherent states in the following.

As detailed in [51], photon wave packets provide various degrees of freedom for information encodings, such as wavefront and polarization. This section exploits photon wave packets' polarization degree of freedom as the information carrier and superscripts the polarization of photon wave packets to highlight the information bit. For example, consider Alice encodes classical bit 0 as the diagonal polarization state of a weak coherent pulse. According to (1) and (8), the emitted state in the preparation stage (1) is specified by $|\psi_D\rangle^{(1)}_{\mathrm{C},1} = \hat{D}(\alpha_1 \zeta_1^D)|0\rangle^{(1)}$, where the subscript 1 is Alice's index, and the superscript D indicates that the polarization of electric mode is diagonal. Therefore, based on the materials of Section III, specifically (19), the quantum state at Bob's receiver port ($j = 2, l = i = 1$), labeled as AB in Fig. 6(a), becomes

$$|\psi_D\rangle^{(3)}_{\mathrm{C},21} \approx \hat{D}(\alpha_1 \bar{\gamma}_{1121})|0\rangle^{(3)}$$

where from (7) $\bar{\gamma}_{1121}(\omega_1) = \mathrm{A}_{2,11}(\omega_1)\mathrm{B}_{21}\zeta_1^D(\omega_1)$ which only contains Alice's transmitted diagonal polarization signal ζ_1^D. Recall that $\zeta_1^D(\omega)$ is a narrowband wave packet with the central frequency ω_1 in the Lambdanet network. Assume Bob's received signal at port AB passes the polarization detection scheme, shown in Fig. 6(b). The 50:50 BS transforms the field operator as $\hat{\mathrm{BS}}^\dagger \hat{a}^{(3)}_{\mathrm{AB},\zeta_1^D} \hat{\mathrm{BS}} = \frac{1}{\sqrt{2}}(\hat{b}_{1,\zeta_1^D} + \hat{b}_{2,\zeta_1^D})$, where $\hat{b}_{1,\zeta_1^D}$ corresponds to the transmission port of the BS and $\hat{b}_{2,\zeta_1^D}$ corresponds to the reflection port. Note that the unitary operator related to the BS as a 2×2 star coupler is indicated by $\hat{\mathrm{BS}}$. The unitary transformation associated with the half-wave plate (H), $\hat{\mathrm{U}}_{\mathrm{H}}$, on the reflected beam from the BS, gives rise to $\hat{\mathrm{U}}_{\mathrm{H}} \hat{b}_{2,\zeta_1^D} \hat{\mathrm{U}}^\dagger_{\mathrm{H}} = \hat{b}_{2,\zeta_1^H}$, where the superscript H shows the horizontal polarization. As a result, the PBS in its horizontal port will experience the transmitted photon with mean photon number $\langle \hat{b}^\dagger_{2,H}(\omega_1)\hat{b}_{2,H}(\omega_1)\rangle = |\frac{1}{\sqrt{2}}\alpha_1 \mathrm{B}_{21}\mathrm{A}_{2,11}(\omega_1)\zeta_1^D(\omega_1)|^2$ [see (18)]. Thus, the single photon detector SPD1 can click with the probability [42], [52], [53]

$$P^{(\mathrm{L})}_{AB} = 1 - \exp\left(-\eta' \int \left|\frac{1}{\sqrt{2}}\alpha_1 \mathrm{B}_{21}\mathrm{A}_{2,11}(\omega)\zeta_1(\omega)\right|^2 d\omega\right)$$
$$\approx \eta' \left|\frac{1}{\sqrt{2}}\alpha_1 \mathrm{B}_{21}\mathrm{A}_{2,11}(\omega_1)\right|^2. \quad (53)$$

Meanwhile, there is a vacuum state in the other port of PBS, and the ideal SPD2, related to vertical polarization, never clicks. Indeed, (53) is the one minus the probability that the vacuum state is in the coherent state distribution. Note that the total efficiency η' comprises the detector efficiency, channel transmittance, and other devices' transmission coefficients in the detection setup from BS toward SPD1 [see Fig. 6(b)]. In (53), it is assumed that the demultiplexer bandwidth ($\Delta\omega_A$) is the same or wider than the laser bandwidth. Moreover, the amplitude $\mathrm{A}_{2,11}(\omega)$ at the laser's spectrum is almost constant and equal to $\mathrm{A}_{2,11}(\omega_1)$. Hence, $\int d\omega |\mathrm{A}_{2,11}(\omega)\zeta_1(\omega)|^2 \approx |\mathrm{A}_{2,11}(\omega_1)|^2 \int d\omega |\zeta_1(\omega)|^2 = |\mathrm{A}_{2,11}(\omega_1)|^2$. If the bandwidth of the demultiplexer's output mode is less than the input laser's, $\zeta_1(\omega)$ will be tailored, and $\int d\omega |\mathrm{A}_{2,11}(\omega)\zeta_1(\omega)|^2 \approx |\mathrm{A}_{2,11}(\omega_1)|^2 \int_{\omega-\Delta\omega_A/2}^{\omega+\Delta\omega_A/2} d\omega |\zeta_1(\omega_1)|^2$, where $\int_{\omega-\Delta\omega_A/2}^{\omega+\Delta\omega_A/2} d\omega |\zeta_1(\omega_1)|^2 < 1$. One can insert this additional loss in the heart of η'.

IEEE Transactions on Quantum Engineering

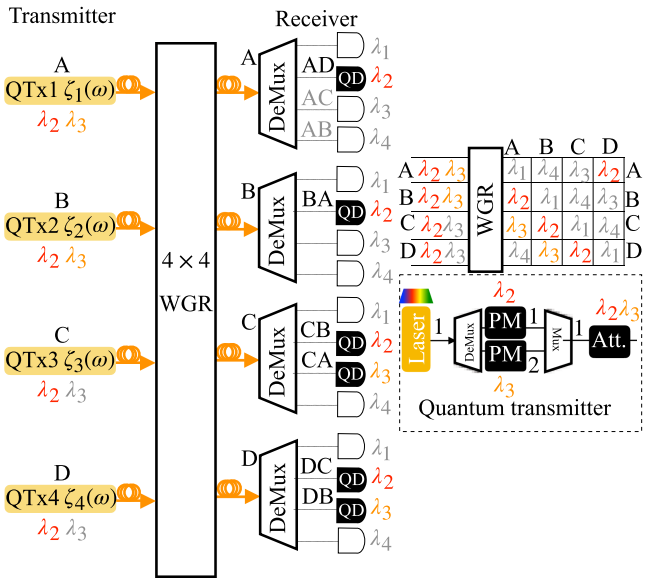

FIGURE 7. Schematic configuration of BB84-QKD based quantum WDM network using WGR among four users, A: Alice, B: Bob, C: Charlie, and D: David. QS is a quantum source. PM is a polarization modulator, and Att. is an attenuator.

B. WGR-BASED QKD NETWORK

As mentioned in Section IV, the introduced loss by WGR is relatively insensitive to increasing the number of users compared to the star coupler in the Lambdanet network. Thus, the QKD network based on WGR is investigated in this subsection.

For a fully connected four-user WGR-based QKD network, Fig. 7 assumes Alice (A) and Bob (B) have quantum sources containing two carrier frequencies, $\omega_2 = 2\pi c/\lambda_2$, and $\omega_3 = 2\pi c/\lambda_3$. At the same time, Charlie (C) and David (D) transmit a narrowband light signal with the central frequency $\omega_2 = 2\pi c/\lambda_2$. On the other hand, Alice and Bob require one detection setup, whereas Charlie and David have two [for a typical detection scheme, see Fig. 6(b)].

According to the table shown in Fig. 7, one can conceive which user plays the role of a quantum transmitter (the table's columns) while the other is a QRx (the table's rows) in each link of the QKD network. For instance, consider Alice and David, who exchange quantum data via a quantum signal with central wavelength λ_2. In this case, David transmits an encoded quantum signal with a narrowband wave packet around the central wavelength λ_2. Meanwhile, Alice receives the signal from the output port of her demultiplexer indicated by AD. The quantum source is at Alice's site in the QKD link between Alice and Bod, and a detection setup is at Bob's port BA. In the same way, all users are linked independently to each other. Therefore, this four-user router-based QKD network only needs two carrier wavelengths λ_2 and λ_3, and each user is equipped with a broadband quantum source and, at most, two detection setups. Assume the quantum sources are weak coherent pulses. Since every QKD link in the network works analogously, we only concentrate on the quantum state evolution between Alice and Bob. The results of other pairs are similar. As illustrated in Fig. 7, Alice transmits two quantum signals with carrier wavelengths λ_2 and λ_3. Thus, the wave-packet $\zeta_1(\omega)$ incorporates two narrowband wave packets, $\xi_1(\omega)$ and $\xi_2(\omega)$, with the central frequencies ω_2 and ω_3, respectively, i.e., $\zeta_1(\omega) = \frac{1}{\sqrt{2}}(\xi_1(\omega) + \xi_2(\omega))$. To avoid crosstalk, the wave-packet $\zeta_1(\omega)$ is prepared such that its nonzero contribution only occurs as

$$\zeta_1(\omega) \approx \begin{cases} \frac{1}{\sqrt{2}}\xi_1(\omega), & |\omega - \omega_2| \le \Delta\omega_A/2 \\ \frac{1}{\sqrt{2}}\xi_2(\omega), & |\omega - \omega_3| \le \Delta\omega_A/2 \end{cases} \tag{54}$$

where $|\omega_2 - \omega_3| \gg \Delta\omega_A$. As shown in the bottom right-hand corner of Fig. 7, Alice's quantum transmitter can provide a polarization-encoded broadband wave packet as follows. First, a broadband laser source is demultiplexed. Then, the polarization of each demultiplexed signal is randomly modulated by a polarization modulator. Finally, the polarization-modulated signals are multiplexed. In line with the material of Appendices A and B, the field creation operator related to the broadband input wave-packet $\zeta_1(\omega) = \frac{1}{\sqrt{2}}(\xi_1(\omega) + \xi_2(\omega))$ (prepared by Alice in Fig. 7) evolves as follows:

$$\begin{aligned} \hat{a}^{\dagger(1)}_{1,\zeta_1^{p_{in}}} &\xrightarrow{\text{DeMux+PM}} \frac{1}{\sqrt{2}}(\hat{a}^{\dagger(1)}_{1,\xi_1^{p_1}} + \hat{a}^{\dagger(1)}_{2,\xi_2^{p_2}}) \\ &\xrightarrow{\text{Mux}} \frac{1}{\sqrt{2}}(\hat{a}^{\dagger(1)}_{1,\xi_1^{p_1}} + \hat{a}^{\dagger(1)}_{1,\xi_2^{p_2}}) \end{aligned} \tag{55}$$

or using (9), the input coherent state evolves as

$$\begin{aligned} \hat{D}_1(\alpha_1'\zeta_1^{p_{in}})|0\rangle^{(1)} &\to \text{DeMux+PM}\hat{D}_1\left(\frac{\alpha_1'}{\sqrt{2}}\xi_1^{p_1}\right) \\ &\quad \times \hat{D}_2\left(\frac{\alpha_1'}{\sqrt{2}}\xi_2^{p_2}\right)|0\rangle^{(1)} \\ &\xrightarrow{\text{Mux}} \hat{D}_1\left(\frac{\alpha_1'}{\sqrt{2}}\xi_1^{p_1}\right)\hat{D}_1\left(\frac{\alpha_1'}{\sqrt{2}}\xi_2^{p_2}\right)|0\rangle^{(1)} \end{aligned} \tag{56}$$

where the superscripts p_{in} and p_1 (p_2) are the input field polarization and the polarization of upper (lower) output ports of the demultiplexer chosen randomly by PMs. For the sake of a better understanding of different signal modes, in (56), the subscript i appears in the displacement operator $\hat{D}_i$ which illustrates the path that each light signal is passing. For example, after demultiplexer, signals with different central frequencies pass through separate paths 1 and 2. The narrowband wave packet around λ_i with polarization p_i is indicated by $\xi_i^{p_i}(\omega)$, where $\int \xi_i^{*p_i}(\omega)\xi_j^{p_j}(\omega)d\omega \approx \delta_{ij}$, and $\zeta_1^{p_i}(\omega_i) \approx \frac{1}{\sqrt{2}}\xi_i^{p_i}(\omega_i)\,\forall i, j \in \{1, 2\}$. Note that each independent field indicated by the creation operator $\hat{a}^{\dagger(1)}_{1,\xi_j^{p_j}}$ is guided to the different receiver j irrespective of its randomly chosen polarization. Hence, Alice communicates independently with the jth receiver. According to (24), the state of signal in the output port of Bob's demultiplexer is associated with the Bob–Alice

links and indicated by BA ($j = 2, l = 2$) in Fig. 7 is

$$|\psi_D\rangle^{(3)}_{\mathrm{C},21} = \hat{D}(\alpha_1' \bar{\gamma}_{2121})|0\rangle^{(3)} \tag{57}$$

provided Alice prepares the coherent signal with diagonal polarization and the mean photon number $|\alpha_1'|^2$, i.e., $|\psi_D\rangle^{(1)}_{\mathrm{C},1} = \hat{D}(\alpha_1' \zeta_1^D)|0\rangle^{(1)}$. Therefore, the dominant value of $\bar{\gamma}_{2121}(\omega)$ happens at the frequency band ω_2 that is $\bar{\gamma}_{2121}(\omega_2) = \mathrm{A}_{2,21}(\omega_2)\mathrm{S}_{21}(\omega_2)\zeta_1^D(\omega_2)$ due to (7) and approximation (46) for AWG. As the 50:50 BS in the detection setup halves the power of the signal, the SPD1 clicks with the probability

$$P_{\mathrm{AB}}^{(\mathrm{R})} = 1 - \exp\left(-\eta' \int_{\omega_2 - \frac{\Delta\omega_A}{2}}^{\omega_2 + \frac{\Delta\omega_A}{2}} d\omega \left|\frac{\alpha_1'}{\sqrt{2}} \mathrm{A}_{2,21}(\omega)\mathrm{S}_{21}(\omega)\zeta_1^D(\omega)\right|^2\right)$$

$$\approx \eta' \int_{\omega_2 - \frac{\Delta\omega_A}{2}}^{\omega_2 + \frac{\Delta\omega_A}{2}} d\omega \left|\frac{\alpha_1'}{\sqrt{2}} \mathrm{A}_{2,21}(\omega)\mathrm{S}_{21}(\omega)\zeta_1^D(\omega)\right|^2 \tag{58}$$

where the total efficiency η' has defined in Section VI-A. The approximation

$$\eta' \int_{\omega_2 - \frac{\Delta\omega_A}{2}}^{\omega_2 + \frac{\Delta\omega_A}{2}} |\frac{\alpha_1'}{\sqrt{2}} \mathrm{A}_{2,21}(\omega)\mathrm{S}_{21}(\omega)\zeta_1^D(\omega)|^2 d\omega \ll 1$$

has been applied in deriving the last line of (58). To further simplify (58), similar to the Lambdanet-based QKD, we assume $\mathrm{S}_{21}(\omega)$ and $\mathrm{A}_{2,21}(\omega)$ are constant along the width of the wave-packet $\zeta_1^D(\omega)$ around the central frequency ω_2. Thus, (58) is estimated as

$$P_{\mathrm{AB}}^{(\mathrm{R})} \approx \eta' |\frac{1}{\sqrt{2}} \mathrm{A}_{2,21}(\omega_2)\mathrm{S}_{21}(\omega_2)|^2 \left| \int_{\omega_2 - \frac{\Delta\omega_A}{2}}^{\omega_2 + \frac{\Delta\omega_A}{2}} \alpha_1' \zeta_1^D(\omega)|^2 d\omega \right|. \tag{59}$$

To compare the Lambdanet-based-QKD with WGR-based QKD, the input intensity of the transmitter source related to each QKD link is assumed to be equal in both topologies. Therefore, according to (54), in the WGR-based QKD, α_1' is adjusted such that

$$\int_{\omega_2 - \frac{\Delta\omega_A}{2}}^{\omega_2 + \frac{\Delta\omega_A}{2}} |\alpha_1' \zeta_1^D(\omega)|^2 d\omega = |\alpha_1'|^2 \int_{\omega_2 - \frac{\Delta\omega_A}{2}}^{\omega_2 + \frac{\Delta\omega_A}{2}} \left|\frac{1}{\sqrt{2}} \xi_1^D(\omega)\right|^2 d\omega$$

$$= |\alpha_1|^2$$

which implies $|\alpha_1'|^2 \approx 2|\alpha_1|^2$, where α_1 is related to the corresponding intensity in the Lambdanet network. This condition can be provided by adding a proper intensity attenuation at Alice's site. As a result

$$P_{\mathrm{AB}}^{(\mathrm{R})} \approx \eta' \left|\frac{\alpha_1}{\sqrt{2}} \mathrm{A}_{2,21}(\omega_2)\mathrm{S}_{21}(\omega_2)\right|^2. \tag{60}$$

Since a weak coherent state contains a multiphoton number state, the crosstalk happening, for example, in WGR outputs, leads to security issues [54]. However, using decoy states, one can estimate the lower bound for a single photon gain and an upper bound for a single photon error of a coherent state distribution, and accordingly, the secure key rate is extracted likewise the point-to-point decoy state BB84 QKD protocol [43].

C. NETWORK SECURE-KEY RATE ESTIMATION

In this section, we evaluate a maximum achievable secure key rate between each pair in each above network topology with the help of the existing practical parameters. The asymptotic secure-key rate for the efficient BB84 QKD without employing decoy states (neglecting photon number splitting attack) is given by [55], [56], and [57] as

$$R = Q[1 - 2H_2(E)] \tag{61}$$

where Q is the gain of the transmitted signal in the receiver's site. The error rate of the decoded information is indicated by E and $H_2(x) = -x\log_2(x) - (1-x)\log_2(1-x)$ is the Shannon entropy. For the Lambdanet-based QKD network and the WGR-based QKD network, the secure-key rate between Alice (A) and Bob (B) is gauged as follows. The related gain for each topology ($\mathscr{L}$=Lambdanet-based, $\mathscr{R}$=Router-based) is the summation of the probability of photon detection at Bob's site due to the sent data by Alice and the detector's dark count as

$$Q_{\mathrm{AB}}^{(\mathscr{L},\mathscr{R})} = P_{\mathrm{AB}}^{(\mathscr{L},\mathscr{R})} + P_d(1 - P_{\mathrm{AB}}^{(\mathscr{L},\mathscr{R})}. \tag{62}$$

The raw key rate per bit by Bob (the probability that Bob's detector clicks after sending a qubit from Alice) is the gain $Q_{\mathrm{AB}}^{(\mathscr{L},\mathscr{R})}$ in (62), which has two contributions: the first one is the probability of receiving data from Alice to Bob, i.e., $P_{\mathrm{AB}}^{(\mathscr{L},\mathscr{R})}$, plus the second one, the probability of dark count detection while there is no photon reaching to Bob from Alice, i.e., $P_d(1 - P_{\mathrm{AB}}^{(\mathscr{L},\mathscr{R})})$. The total raw key rate at Bob's site is the product of this gain to Alice's sending bit rate of data, limited, e.g., by the modulation rate of the laser. The raw key rate is the rate before any postprocessing.

The error rate appearing in (61) is given by

$$E_{\mathrm{AB}}^{(\mathscr{L},\mathscr{R})} = \frac{P_{\mathrm{AB}}^{(\mathscr{L},\mathscr{R})}\mathscr{E} + 1/2P_d(1 - P_{\mathrm{AB}}^{(\mathscr{L},\mathscr{R})})}{Q_{\mathrm{AB}}^{(\mathscr{L},\mathscr{R})}} \tag{63}$$

where $\mathscr{E}$ is a free error probability, including all possible inline errors, such as the network crosstalk or misalignment of polarization preparation and detection schemes. By assuming SPD are polarization-insensitive, their dark count probability P_d introduces erroneous data with the probability of $1/2$. For obtaining a nonzero key rate R from (61), the error E should be less than 11% (Note that $H_2(11\%) = 1/2$,

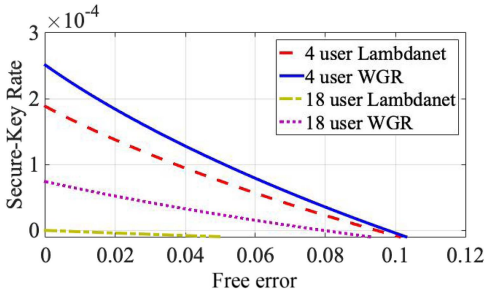

FIGURE 8. Secure key rate subject to free error of QKD in the Lambdanet (dashed-red and dashed-dot-yellow) and WGR-based (solid-blue and dot-purple) WDM network.

therefore, for this erros $R = 0.$). Thus, this tolerable amount of E has limited the admissible crosstalk in the quantum network. As is clear from (63), the total error rate $E_{\mathrm{AB}}^{(\mathscr{L},\mathscr{R})}$ observed from the detected data at Bob's site comes from two terms: 1) the error on the received data from Alice and 2) the bit error due to the dark count. Note that the detector's dark count with the probability of $1/2$ leads to the bit error in the received data. Each of these terms is multiplied by Bob's fraction of the related received rate per the total gain ($Q_{\mathrm{AB}}^{(\mathscr{L},\mathscr{R})}$). For a four-user QKD network where $|B_{21}|^2 = 1/4$ and $|\mathrm{S}_{21}|^2 = 0.32$ [58], according to (53) and (60)

$$\frac{P_{\mathrm{AB}}^{\mathrm{R}}}{P_{\mathrm{AB}}^{\mathrm{L}}} = \frac{|\mathrm{S}_{21}|^2}{|B_{21}|^2} \approx 1.26. \tag{64}$$

This indicates the WGR-based QKD network's superiority over the Lambdanet-based QKD network. This advantage becomes more noticeable as the number of users increases. For instance, for 18-user QKD network the ratio $P_{\mathrm{AB}}^{\mathrm{R}}/P_{\mathrm{AB}}^{\mathrm{L}} \approx 3.6$ where $|B_{21}|^2 = 1/18$ and $|\mathrm{S}_{21}|^2 = 0.2$ (see [45, Fig. 5] and its peak on 3.5 dB which is equivalent to $|\mathrm{S}_{21}|^2 = 0.2$). Fig. 8 shows the secure-key rate R versus free error $\mathscr{E}$. To sketch this plot, we only consider the channel transmittance ($10^{(-\bar{\alpha}\mathscr{L}/10)}$) and the detector efficiency η in η' and dismiss other possible sources of loss. So, $\eta' = \eta 10^{(-\bar{\alpha}\mathscr{L}/10)}$ where $\mathscr{L} = 10$ km is the length of the single mode fiber between Alice and Bob with the loss coefficient $\bar{\alpha} = 0.2$ dB/km, and $\eta = 10\%$ is the efficiency of a typical single photon detector with dark count probability $P_d = 10^{-5}$. The sensitivity of the mode conversion process to the input polarization state is indeed an important factor that must be carefully considered in practical quantum networks. In particular, polarization controllers play a crucial role in mitigating these effects, ensuring stable operation in applications, such as QKD, where maintaining polarization integrity is essential for secure communication. Addressing polarization dependence is key to enhancing the versatility and robustness of quantum photonic systems; however, it is beyond the scope of this work.

VII. CONCLUSION

This article details several quantum WDM network architectures following the systematic and unified approach of a generic quantum WDM communication system presented in [13].

We study the Lambdanet-based quantum network as a fully connected QWDM communication system. We investigate the quantum version of the conventional Lambdanet topology via quasi-classical (coherent) state inputs. We show that, as expected, there is no quantum correlation between the quantum states of different receivers. Indeed, the total state is the tensor product of coherent states with modified wave packets. At the same time, we explore the truly secured quantum version of the Lambdanet through single-photon sources. We derive the output intensity and the collapsed output state after the projective measurement of the received signals for the network. Employing single-photon sources introduces a quantum correlation between receivers' states.

Then, we investigate Router-based quantum WDM communication networks. These networks deterministically route the signal to the desired receiver to avoid broadcasting and photon loss. Photon loss hinders quantum communication networks due to the weakness of quantum signals. The WGR-based network can establish pairwise links among all users simultaneously. The network's performance is analyzed while the transmitters' sources are coherent, broadband single-photon, and multiplexed narrowband single-photon states. Similarly, feeding the network with coherent states leads to uncorrelated final states at the receivers' sites. Moreover, the topology can introduce an uncorrelated state at the receiver's outputs, provided that the WGR is lossless and fed with single-photon states as inputs.

Furthermore, we introduce FTTQ receiver architecture, inheriting its structure from the conventional FTTH technology. In this respect, we investigated the evolution of narrowband single-photon and coherent signals through a wavelength distributor, combining a quantum multiplexer, a lossy optical fiber, and a quantum demultiplexer. The mathematical quantum model of the wavelength distributer connecting N users is studied via the $2N \times 2N$ quantum unitary operator. FTTQ establishes quantum links by devoting distinct wavelengths to each pair of quantum users and an efficient routing mechanism.

Finally, we examine Lambdanet and WGR-based networks for QKD applications. We discuss the number of required quantum sources, detectors, and dedicated wavelengths for each. The secure key rate analysis shows that the WGR-based topology outperforms the Lambdanet topology; specifically, when the number of users increases, the difference in the QKD communication rate is significant.

Maintaining quantum coherence throughout a QWDM network is indeed challenging due to factors like crosstalk and signal loss. However, the mathematical framework presented in our work offers strategies to address these issues. Specifically, our methodology facilitates the characterization of device parameters, identifying and mitigating crosstalk and loss within the network. Future research can leverage

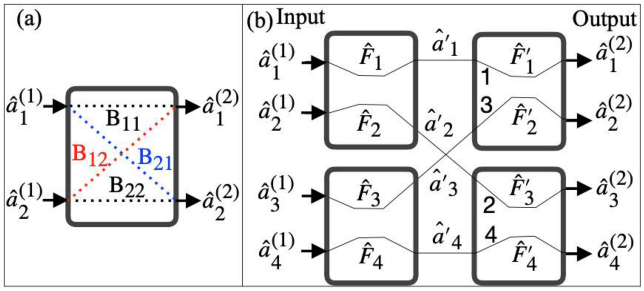

FIGURE 9. (a) 2 × 2 star coupler formed by a 3dB-fiber coupler (2 × 2 balanced BS). (b) 4 × 4 star coupler formed by four 3dB-fiber couplers. Note that in the schematic of the 2 × 2 star coupler (a), B_{11} and B_{22} (B_{21} and B_{12}) are assumed to be reflection (transmission) coefficients.

this framework to optimize device designs and network configurations, thereby enhancing the preservation of quantum coherence in QWDM systems.

APPENDIX A
QUANTUM STAR COUPLER

As mentioned in Section III, a generic wavelength distributor can be a star coupler whose related unitary operator is identified by $\hat{G} = \hat{B}$. A balanced star coupler combines N input signals from transmitters and splits up equally among all receivers. Fig. 9(a) and (b) depict 2 × 2 and 4 × 4 star couplers realized by 3-dB-fiber couplers, respectively. The unitary quantum transformation corresponding to a 2 × 2 star coupler shown in Fig. 9(a) can be understood by input–output relations of an ideal lossless BS as follows [59]:

$$\begin{aligned}\hat{a}_1^{(2)}(\omega) &= \mathrm{B}_{11}(\omega)\hat{a}_1^{(1)}(\omega) + \mathrm{B}_{12}(\omega)\hat{a}_2^{(1)}(\omega)\\ \hat{a}_2^{(2)}(\omega) &= \mathrm{B}_{21}(\omega)\hat{a}_1^{(1)}(\omega) + \mathrm{B}_{22}(\omega)\hat{a}_2^{(1)}(\omega)\end{aligned} \tag{65}$$

where $\hat{a}_1^{(1)}(\omega)$ and $\hat{a}_2^{(1)}(\omega)$ ($\hat{a}_1^{(2)}(\omega)$ and $\hat{a}_2^{(2)}(\omega)$) are annihilation operators of input (output) fields. BS reflection and transmission coefficients are $\mathrm{B}_{11}(\omega) = \mathrm{B}_{22}^*(\omega) = r(\omega)$ and $\mathrm{B}_{21}(\omega) = -\mathrm{B}_{12}^*(\omega) = t(\omega)$, respectively [60].

Due to the unitary evolution connecting input modes to output modes of lossless BSs, the reflection and transmission coefficients of lossless BSs are restricted as

$$\begin{aligned}|r(\omega)|^2 + |t(\omega)|^2 &= 1\\ r(\omega)t^*(\omega) + t(\omega)r^*(\omega) &= 0.\end{aligned} \tag{66}$$

Employing (66), the commutation relations between output creation and annihilation operators will be preserved. For a concrete example, the input–output relation of the frequency-independent balanced BS as a 2 × 2 star coupler can be written as

$$\begin{aligned}\begin{bmatrix}\hat{a}_1^{(2)}(\omega)\\ \hat{a}_2^{(2)}(\omega)\end{bmatrix} &= \underline{\mathrm{B}}\begin{bmatrix}\hat{a}_1^{(1)}(\omega)\\ \hat{a}_2^{(1)}(\omega)\end{bmatrix}\\ &= \frac{1}{\sqrt{2}}\begin{bmatrix}1 & i\\ i & 1\end{bmatrix}\begin{bmatrix}\hat{a}_1^{(1)}(\omega)\\ \hat{a}_2^{(1)}(\omega)\end{bmatrix}\end{aligned} \tag{67}$$

where $\underline{\mathrm{B}}$ is a 2 × 2 unitary scattering matrix satisfying the conditions in (66). The generalized form of (67) pertains to the $N \times N$ star coupler introduces the following input–output relation [40]:

$$\vec{\hat{a}}^{(2)}(\omega) = \underline{\mathrm{B}}_{N\times N}\vec{\hat{a}}^{(1)}(\omega) \tag{68}$$

where

$$\begin{aligned}\vec{\hat{a}}^{(1)}(\omega) &= (\hat{a}_1^{(1)}(\omega), \cdots, \hat{a}_N^{(1)}(\omega))^{\mathrm{T}}\\ \vec{\hat{a}}^{(2)}(\omega) &= (\hat{a}_1^{(2)}(\omega), \ldots, \hat{a}_N^{(2)}(\omega))^{\mathrm{T}}.\end{aligned}$$

Superscript T stands for transpose. For the balanced star coupler, $\underline{\mathrm{B}}_{N\times N}$ is the $N \times N$ coefficient matrix in which the absolute value of the matrix component becomes

$$|\mathrm{B}_{ij}| = (1/\sqrt{N}). \tag{69}$$

For the more general case, since $\underline{\mathrm{B}}(\omega)$ is a unitary $N \times N$ matrix, the input modes can be written with respect to the output modes as

$$\vec{\hat{a}}^{(1)} = \underline{\mathrm{B}}^{\dagger}_{N\times N}(\omega)\vec{\hat{a}}^{(2)}. \tag{70}$$

For the transformation represented in (68), there exists the unitary operator $\hat{\mathrm{B}}$ (acting on the related Hilbert space) such that

$$\vec{\hat{a}}^{(2)} = \underline{\mathrm{B}}(\omega)\vec{\hat{a}}^{(1)} := \hat{\mathrm{B}}\vec{\hat{a}}^{(2)}\hat{\mathrm{B}}^{\dagger} \tag{71a}$$

$$\vec{\hat{a}}^{(1)} = \underline{\mathrm{B}}^{\dagger}(\omega)\vec{\hat{a}}^{(2)} := \hat{\mathrm{B}}^{\dagger}\vec{\hat{a}}^{(1)}\hat{\mathrm{B}} \tag{71b}$$

where the unitary relation $\hat{\mathrm{B}}^{\dagger}\hat{\mathrm{B}} = \hat{\mathrm{B}}\hat{\mathrm{B}}^{\dagger} = I$ is used to derive (71b). Therefore, based on the Schrödinger picture, the input state $|\psi\rangle^{(1)}$ evolves as $|\psi\rangle^{(2)} = \hat{\mathrm{B}}^{\dagger}|\psi\rangle^{(1)}$ [61].

Note that according to (68) and (69), the lossless $N \times N$ balanced star coupler reduces the power of each input (classical intensity) by the factor $(1/N)$.

A. LOSSY STAR COUPLER

As Fig. 9(b) shows, a combination of several BSs can fabricate the star coupler. Therefore, studying a lossy star coupler by quantum mechanical formalism suffices to revisit the lossy BS. For a fully quantum mechanical view of the evolution of an electrical field in a lossy BS when a light beam interacts with a dielectric medium with complex transmission and reflection coefficients, both field and medium must be quantized as degrees of freedom of the compound system. Analyzing a fully canonical quantization scheme for the light field in dispersive and lossy linear dielectric was carried out by [62]. Nevertheless, more simply, studying the input and output fields far from the lossy BS with the help of Langevin equations was performed in [63] is followed in this article. In the presence of loss, (66) are transformed to the inequalities

$$|r(\omega)|^2 + |t(\omega)|^2 \le 1 \tag{72}$$

$$|r(\omega)t^*(\omega) + t(\omega)r^*(\omega)| \le 1 - |r(\omega)|^2 - |t(\omega)|^2. \tag{73}$$

IEEE Transactions on Quantum Engineering

The following equations give the general relationships between input–output annihilation operators of the optical field passing through a lossy symmetric BS ($B_{12} = B_{21} = t$, $B_{11} = B_{22} = r$) [63], [64]

$$\hat{a}_1^{(2)}(\omega) = r(\omega)\hat{a}_1^{(1)}(\omega) + t(\omega)\hat{a}_2^{(1)}(\omega) + \hat{F}_1(\omega)$$
$$\hat{a}_2^{(2)}(\omega) = t(\omega)\hat{a}_1^{(1)}(\omega) + r(\omega)\hat{a}_2^{(1)}(\omega) + \hat{F}_2(\omega) \quad (74)$$

where $\hat{F}_i(\omega)$ for $i \in \{1, 2\}$ are Langevin noise operators which satisfy the commutation relations

$$[\hat{F}_i(\omega), \hat{F}_i^{\dagger}(\omega')] = \delta(\omega - \omega')\{1 - |r(\omega)|^2 - |t(\omega)|^2\} \quad (75)$$

$$\left[\hat{F}_i(\omega), \hat{F}_j^{\dagger}(\omega')\right] = -\delta(\omega-\omega')\{r(\omega)t^*(\omega)+t(\omega)r^*(\omega)\}\, i \neq j. \quad (76)$$

The noise operators $\hat{F}_i(\omega)$ describe fluctuating currents in the dielectric forming a BS, and their appearance in (74) gives rise to preserving the commutation relations between creation and annihilation operators of input-output fields [65]. At optical frequency, the quantum state of the medium can be assumed in its ground state. So in all the following calculations, the effect of Langevin noise operators on the input state of the composite system ($|0\rangle_{\text{com}}$), which contains both the vacuum state of the input fields and the ground state of the absorbing medium, becomes zero, i.e., $\hat{F}_1(\omega)|0\rangle_{\text{com}} = \hat{F}_2(\omega)|0\rangle_{\text{com}} = \hat{a}_1^{(1)}|0\rangle_{\text{com}} = \hat{a}_2^{(1)}|0\rangle_{\text{com}} = 0$. Note that $\hat{F}_i$ and $\hat{a}_i^{(1)}$ are independent modes which means $[\hat{F}_i, \hat{a}_j^{(1)}] = 0\,\forall i, j$. For simplicity, we assume the reflection and transmission coefficients of the star coupler are frequency-independent, and discrete optical modes are taken into account [e.g., by considering the BS (dielectric) is put inside an optical cavity]. Calculation of the normally ordered characteristic function is a helpful tool to evaluate the effect of loss on the average of the photon number received by each user from the related output port of the BS, i.e., $\langle \hat{a}_j^{\dagger(2)}\hat{a}_j^{(2)}\rangle$ where $j \in \{1, 2\}$. The normally ordered characteristic function χ_k for two modes is written as

$$\chi_k[\xi_1, \xi_2] = \langle e^{\xi_1\hat{a}_1^{\dagger(k)}} e^{\xi_2\hat{a}_2^{\dagger(k)}} e^{-\xi_1^*\hat{a}_1^{(k)}} e^{-\xi_2^*\hat{a}_2^{(k)}}\rangle \quad (77)$$

where $k \in \{1, 2\}$ indicates that the characteristic function is for the input (1) or output (2) modes. Using (74) and given the medium is in the vacuum state (i.e., $|0\rangle_m$), it is straightforward to show

$$\chi_2[\xi_1, \xi_2] = \chi_1[r^*\xi_1 + t^*\xi_2, t^*\xi_1 + r^*\xi_2]. \quad (78)$$

Note that $\hat{F}_i|0\rangle_m = 0$. Therefore, with the help of the characteristic function, the average photon number for the jth output yields

$$\langle \hat{a}_j^{\dagger(2)}\hat{a}_j^{(2)}\rangle = -\frac{\partial^2}{\partial\xi_j\partial\xi_j^*}\chi_2[\xi_1, \xi_2]|_{\xi_1=\xi_2=0}. \quad (79)$$

Provided the single photon state $|\psi_i\rangle = \hat{a}_i^{\dagger(1)}|0\rangle$ is prepared by the ith input, $\langle \hat{a}_j^{\dagger(2)}\hat{a}_j^{(2)}\rangle = |t|^2 + |r|^2 \leq 1$ (which is less than one due to the lossy star coupler).

For a lossy 4×4 star coupler as depicted in Fig. 9(b), the Langevin equations are rewritten as

$$\hat{a}_1' = r\hat{a}_1^{(1)} + t\hat{a}_2^{(1)} + \hat{F}_1, \quad \hat{a}_1^{(2)} = r\hat{a}_1' + t\hat{a}_3' + \hat{F}_1'$$
$$\hat{a}_2' = t\hat{a}_1^{(1)} + r\hat{a}_2^{(1)} + \hat{F}_2, \quad \hat{a}_2^{(2)} = t\hat{a}_1' + r\hat{a}_3' + \hat{F}_2'$$
$$\hat{a}_3' = r\hat{a}_3^{(1)} + t\hat{a}_4^{(1)} + \hat{F}_3, \quad \hat{a}_3^{(2)} = r\hat{a}_2' + t\hat{a}_4' + \hat{F}_3'$$
$$\hat{a}_4' = t\hat{a}_3^{(1)} + r\hat{a}_4^{(1)} + \hat{F}_4, \quad \hat{a}_4^{(2)} = t\hat{a}_2' + r\hat{a}_4' + \hat{F}_4'. \quad (80)$$

According to (80), the compact form of the Langevin equations for the 4×4 star coupler becomes

$$\begin{bmatrix}\hat{a}_1^{(2)}\\ \hat{a}_2^{(2)}\\ \hat{a}_3^{(2)}\\ \hat{a}_4^{(2)}\end{bmatrix} = \begin{bmatrix}r^2 & rt & rt & t^2\\ tr & t^2 & r^2 & rt\\ rt & r^2 & t^2 & rt\\ t^2 & rt & rt & r^2\end{bmatrix}\begin{bmatrix}\hat{a}_1^{(1)}\\ \hat{a}_2^{(1)}\\ \hat{a}_3^{(1)}\\ \hat{a}_4^{(1)}\end{bmatrix} + \begin{bmatrix}r & 0 & t & 0\\ t & 0 & r & 0\\ 0 & r & 0 & t\\ 0 & t & 0 & r\end{bmatrix}\begin{bmatrix}\hat{F}_1\\ \hat{F}_2\\ \hat{F}_3\\ \hat{F}_4\end{bmatrix} + \begin{bmatrix}\hat{F}_1'\\ \hat{F}_2'\\ \hat{F}_3'\\ \hat{F}_4'\end{bmatrix} \quad (81)$$

where $\hat{F}_i$ and $\hat{F}_i'$ are Langevin noise operators of two left-hand side BSs and two right-hand side BSs, as shown in Fig. 9(b). Since the effect of these noise operators on the composite ground state is zero, they do not contribute to calculating the characteristic function. In line with (81), the normally- ordered characteristic function of the 4×4 star coupler output modes in terms of input modes is

$$\begin{aligned}\chi_2[\xi_1, \xi_2, \xi_3, \xi_4] &= \langle e^{\sum_{i=1}^4 \xi_i\hat{a}_i^{\dagger(2)}} e^{-\sum_{i=1}^4 \xi_i^*\hat{a}_i^{(2)}}\rangle\\ &= \chi_1[\eta_1 = r^{*2}\xi_1 + t^*r^*\xi_2 + t^*r^*\xi_3 + t^{*2}\xi_4\\ &\quad \eta_2 = t^*r^*\xi_1 + t^{*2}\xi_2 + r^{*2}\xi_3 + t^*r^*\xi_4\\ &\quad \eta_3 = t^*r^*\xi_1 + r^{*2}\xi_2 + t^{*2}\xi_3 + t^*r^*\xi_4\\ &\quad \eta_4 = t^{*2}\xi_1 + t^*r^*\xi_2 + t^*r^*\xi_3 + r^{*2}\xi_4]\\ &= \langle e^{\sum_{i=1}^4 \eta_i\hat{a}_i^{\dagger(1)}} e^{-\sum_{i=1}^4 \eta_i^*\hat{a}_i^{(1)}}\rangle. \end{aligned} \quad (82)$$

It is worthwhile to study two particular cases, single-photon and coherent (Glauber) states, as inputs of the star couplers. In the former case, for single photon state $|\psi\rangle_S = \prod_{i=1}^4 \hat{a}_i^{\dagger(1)}|0\rangle_i^{(1)} = |1111\rangle$ as inputs of the 4×4 star coupler, the mean photon number in each output becomes

$$\begin{aligned}\langle \hat{a}_j^{\dagger(2)}\hat{a}_j^{(2)}\rangle &= -\frac{\partial^2}{\partial\xi_j\partial\xi_j^*}\chi_2[\xi_1, \xi_2, \xi_3, \xi_4]|_{\xi_1=\xi_2=\xi_3=\xi_4=0}\\ &= (|t|^2 + |r|^2)^2. \end{aligned} \quad (83)$$

For instance, using (82), (83) for $j = 1$ becomes

$$\begin{aligned}\langle \hat{a}_1^{\dagger(2)}\hat{a}_1^{(2)}\rangle = \langle 1111|(&r^{*2}\hat{a}_1^{\dagger(1)} + t^*r^*\hat{a}_2^{\dagger(1)} + t^*r^*\hat{a}_3^{\dagger(1)}\\ &+ t^{*2}\hat{a}_4^{\dagger(1)})(r^2\hat{a}_1^{(1)} + tr\hat{a}_2^{(1)} + tr\hat{a}_3^{(1)}\\ &+ t^2\hat{a}_4^{(1)})|1111\rangle \end{aligned}$$

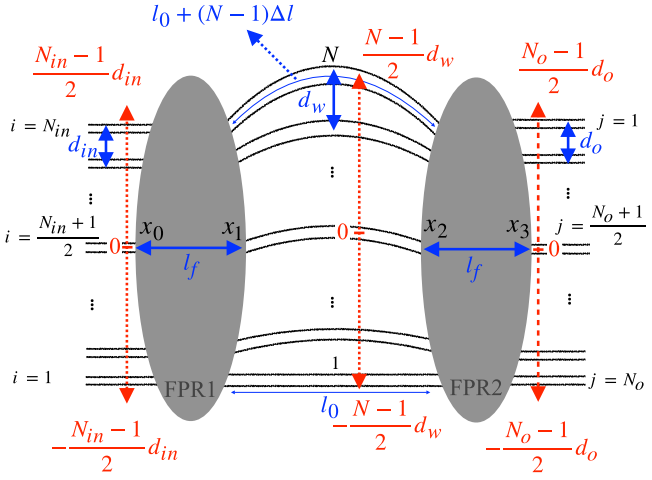

FIGURE 10. **Building blocks of AWG.**

$$= (|t|^2 + |r|^2)^2. \tag{84}$$

The detailed procedures to reach (84) are as follows. First apply derivative with respect to ξ_1 on (82) which leads to the appearance of the summation of creation operators $(r^{*2}\hat{a}_1^{\dagger(1)} + t^*r^*\hat{a}_2^{\dagger(1)} + t^*r^*\hat{a}_3^{\dagger(1)} + t^{*2}\hat{a}_4^{\dagger(1)})$ multiplied by the exponential term $e^{\sum_{i=1}^4 \eta_i \hat{a}_i^{\dagger(1)}}$ and then apply derivative with respect to ξ_1^* on the previous result which leads to the appearance of the summation of annihilation operators $(r^2\hat{a}_1^{(1)} + tr\hat{a}_2^{(1)} + tr\hat{a}_3^{(1)} + t^2\hat{a}_4^{(1)})$ multiplied by the exponential term $e^{-\sum_{i=1}^4 \eta_i^* \hat{a}_i^{(1)}}$. Both exponential terms become identity at $\xi_1 = \xi_2 = \xi_3 = \xi_4 = 0$. Consider the input of the 4×4 star coupler is the coherent state $|\psi\rangle_C = \prod_{i=1}^4 \hat{D}(\alpha_i)|0\rangle^{(1)}$, where $\hat{D}(\alpha_i) = \exp[\alpha_i\hat{a}_i^{\dagger(1)} - \alpha_i^*\hat{a}_i^{(1)}]$. Assuming $\alpha_i = \alpha\, \forall i \in \{1, \ldots, 4\}$, it is easy to show that the coherent state $|\psi\rangle_C$ is still the eigenstate of the output mode $\hat{a}_i^{(2)}$ with eigenvalue $(r^2 + rt + rt + t^2)\alpha$ (apply $|\psi\rangle_C$ on (81) and note that since Langevin noise operators apply to the medium's ground state, they will be excluded from calculation). Therefore, the mean photon value related to output mode $\hat{a}_i^{(2)}$ becomes $\langle \hat{a}_i^{\dagger(2)}\hat{a}_i^{(2)}\rangle = |(r+t)^2|^2|\alpha|^2$.

As a result, by increasing the number of users, the received mean photon number also decreases due to loss in the star coupler. Since the amount of introduced loss is an essential issue in the quantum domain, this issue must be considered when implementing any proposed quantum network.

APPENDIX B
QUANTUM ARRAYED WAVEGUIDE GRATING

As mentioned in Section IV, a generic wavelength distributor can be an arrayed waveguide grating where the unitary operator is identified by $\hat{\mathrm{G}} = \hat{\mathrm{A}}$ for a lossless case and $\hat{\mathrm{G}} = \hat{\mathrm{S}}$ for a lossy one. Furthermore, QRx are lossless AWGs $\hat{\mathrm{QR}} = \hat{\mathrm{A}}$. The building block of an AWG is shown in Fig. 10. It consists of an array of N planar waveguides linked to N_{in} input and N_o output waveguides via two free propagation regions (FPR) in the lens forms, where index in and o correspond to input and output, respectively (assuming $N_{\text{in}} = N_o = N$). The input signal becomes divergent in the first FPR1 ($x_0 \to x_1$). Consequently, the diverged field is coupled to all the arrayed waveguides. Due to the different lengths of the arrayed waveguides in the middle of Fig. 10, the expanded input signal experiences different wavelength-dependent phase shifts along the different arrayed waveguides. The different length between any two adjacent waveguides is fixed to $\Delta l = \frac{m\tilde{\lambda}_0}{n_w}$, where $\tilde{\lambda}_0$ is the design wavelength of the AWG, m is the order of grating, and n_w is the refraction index of waveguides. Finally, the second FPR2 focuses the spectrally separated signal beam at the distinct point on the plane x_3 ($x_2 \to x_3$). Distances d_{in}, d_o, and d_w are fixed parameters that indicate the spaces between input, output, and arrayed waveguides, respectively. According to [15], [45], and [46] with the defined parameters depicted in Fig. 10, the elements of the AWG transfer matrix ($\underline{\mathrm{A}}$) are derived by

$$\mathrm{A}_{ij}(\omega) = e^{-i\Psi_0(\omega)} \iint_{-\infty}^{+\infty} dx_3 dx_0 b_{out}\left(x_3 - \left(\frac{N+1}{2} - j\right) d_o\right) \times K(x_3, x_0|\omega) b_{in}\left(x_0 - \left(i - \frac{N+1}{2}\right) d_{in}\right) \tag{85}$$

in which $\Psi_0(\omega) = \omega n_w(l_0 + \tilde{\lambda}_0 mN/2)/c$ (c is the speed of light in vacuum) is the overall phase shift corresponding to the shortest length of the waveguide in the array, and the integral kernel is

$$K(x_3, x_0|\omega) = \sum_{r=-\infty}^{\infty} e^{\frac{-irn_w\omega\Delta l}{c}} \iint_{-(\frac{N-1}{2})d_w}^{+(\frac{N-1}{2})d_w} \frac{dx_2}{\sqrt{\alpha_\omega}} \frac{dx_1}{\sqrt{\alpha_\omega}} \times b_g(x_2 - rd_w) e^{\frac{-i2\pi x_3 x_2}{\alpha_\omega}} b_g(x_1 - rd_w) e^{\frac{-i2\pi x_1 x_0}{\alpha_\omega}}. \tag{86}$$

The integral kernel $K(x_3, x_0|\omega)$ involves two Fourier transforms related to both FPRs FPR1 and FPR2, respectively, from the curvatures $x_0 \to x_1$ and $x_2 \to x_3$. In both regions, the distances between these curvatures are coincidence with the focal length l_f, and the Fraunhofer diffraction condition is satisfied since $l_f \gg \frac{\pi W_x^2}{4\lambda}$ guarantees Fraunhofer diffraction for typical waveguide width W_x. The wavelength (λ) focal length (l_f) product in Fourier optics propagation is $\alpha_\omega = 2\pi c l_f/(n_s\omega) = \lambda l_f/n_s$ ($\lambda = \frac{2\pi c}{\omega}$), where n_s is the refraction index in FPRs. The spatial mode profiles of input, output, and arrayed waveguides are $b_{\text{in}}(x)$, $b_{\text{out}}(x)$, and $b_g(x)$, respectively. The index of each waveguide in the array is indicated by r, and the finite number of these waveguides (N) is represented in the limits of integration. The first exponential term on the right-hand side of (86) pertains to the phase shift

IEEE Transactions on Quantum Engineering

between waveguides in the array. By assuming the similar input and output waveguides, i.e., $b_{\text{in}}(x) = b_{\text{out}}(x)$ since the AWG becomes symmetric, $\mathrm{A}'_{ij} = e^{i\Psi_0}\mathrm{A}_{ij}(\omega)$ is self-adjoint. Hence, the coefficient matrix with the elements given by (85), except for the common exponential factor $(e^{-i\Psi_0})$, is a Hermitian matrix. Since the AWG is assumed to be lossless and symmetric, the energy conservation condition imposes the related transform matrix to be unitary. To derive the explicit form of ω_{ij}, the dominant frequency passing through the input port j toward the output port i, the spatial mode profile of each waveguide is approximated by delta functions as $b_{\text{in}}(x) = b_{\text{out}}(x) = b_g(x) = \delta(x)$. Substituting this approximation to (85) and (86) yields

$$\mathrm{A}_{ij}(\omega) = e^{-i\Psi_0(\omega)} \sum_{r=-\infty}^{\infty} e^{-ir[\frac{n_w \Delta l}{c}\omega]} e^{-ir[\frac{2\pi d_w d}{\alpha_\omega}(i-j)]} \tag{87}$$

where we have assumed $d_{\text{in}} = d_o = d$. According to [46], by considering the approximation $\alpha_\omega \approx \alpha_{\omega_0} = 2\pi c l_f/(n_s\omega_0)$, where $\omega - \omega_0 \ll \omega_0$ and $\omega_0 = 2\pi c/\tilde{\lambda}_0$ is the carrier frequency related to the design frequency of AWG, (87) is estimated as

$$\begin{aligned}
\mathrm{A}_{ij}(\omega) &\approx e^{-i\Psi_0(\omega)} \sum_{r=-\infty}^{\infty} e^{-ir[\frac{n_w \Delta l}{c}\omega]} e^{-ir[\frac{2\pi d_w d}{\alpha_{\omega_0}}(i-j)]} \\
&= e^{-i\Psi_0(\omega)} \sum_{r=-\infty}^{\infty} e^{-i2\pi r \frac{(\omega + \omega_T \frac{d_w d(i-j)}{\alpha_{\omega_0}})}{\omega_T}} \\
&= e^{-i\Psi_0(\omega)} \omega_T \sum_{r=-\infty}^{\infty} \delta\left(\omega + \omega_T \frac{d_w d(i-j)}{\alpha_{\omega_0}} - r\omega_T\right)
\end{aligned} \tag{88}$$

where $\omega_T = 2\pi c/(n_w \Delta l)$. To derive line three from line two of (88), the following relation is employed:

$$\sum_{r=-\infty}^{\infty} e^{-i2\pi r \frac{\omega}{\omega_T}} = \omega_T \sum_{r=-\infty}^{\infty} \delta(\omega - r\omega_T). \tag{89}$$

The maximums of (88) occurs at the frequencies

$$\omega_{ji} = \frac{c}{\Delta l n_w}\left\{2\pi r - \frac{2\pi d_w d}{\alpha_{\omega_0}}(i-j)\right\},\ r \in \mathbb{Z}. \tag{90}$$

To derive the (90), we set the argument of the Dirac delta function equal to zero. Without approximating α_ω, (87) is rearranged as

$$\begin{aligned}
\mathrm{A}_{ij}(\omega) &= e^{-i\Psi_0(\omega)} \sum_{r=-\infty}^{\infty} e^{-ir\omega[\frac{n_w \Delta l}{c} + \frac{d_w d n_s}{c l_f}(i-j)]} \\
&= e^{-i\Psi_0(\omega)} \sum_{r=-\infty}^{\infty} e^{-i2\pi r \frac{\omega}{\omega'_T}} \\
&= e^{-i\Psi_0(\omega)} \omega'_T \sum_{r=-\infty}^{\infty} \delta(\omega - r\omega'_T)
\end{aligned} \tag{91}$$

where it peaks at frequencies

$$\begin{aligned}
\omega_{ji} &= r\omega'_T \\
&= 2\pi r\left[\frac{n_w \Delta l}{c} + \frac{n_s d_w d}{l_f c}(i-j)\right]^{-1},\quad r \in \mathbb{Z}.
\end{aligned} \tag{92}$$

As it is clear from (90) and (92), for different i and j indexes, whenever $i - j$ is constant, the AWG-guided frequency is the same for all related paths. One can realize ω_{ji} as the frequency of the ith input waveguide guided to the jth output waveguide. The quantum model for the AWG was studied in [45]. The input–output relation between annihilation quantum field operators at frequency ω of a lossless AWG at the input and output of waveguides is

$$\vec{\hat{a}}^{(2)}(\omega) = \underline{\mathrm{A}}_{N\times N}(\omega)\vec{\hat{a}}^{(1)}(\omega) \tag{93}$$

where $\underline{\mathrm{A}}_{N\times N}(\omega)$ is a unitary frequency-dependent $N \times N$ transfer matrix introduced in (85) and the number of specific guided frequency passing from AWG is N. Therefore, the input annihilation operators can also be written according to output modes as

$$\vec{\hat{a}}^{(1)}(\omega) = \underline{\mathrm{A}}^{\dagger}_{N\times N}(\omega)\vec{\hat{a}}^{(2)}(\omega) \tag{94}$$

where

$$\begin{aligned}
\vec{\hat{a}}^{(1)}(\omega) &= (\hat{a}^{(1)}_1(\omega), \ldots, \hat{a}^{(2)}_N(\omega))^{\mathrm{T}} \\
\vec{\hat{a}}^{(2)}(\omega) &= (\hat{a}^{(2)}_1(\omega), \ldots, \hat{a}^{(2)}_N(\omega))^{\mathrm{T}}
\end{aligned}$$

and $(\underline{\mathrm{A}}^{\dagger})_{ij} = \mathrm{A}^*_{ji}$. Furthermore, one can find unitary evolution operator $\hat{\mathrm{A}}$ [45], satisfying the following relation:

$$\vec{\hat{a}}^{(2)} = \underline{\mathrm{A}}(\omega)\vec{\hat{a}}^{(1)} := \hat{\mathrm{A}}\vec{\hat{a}}^{(2)}\hat{\mathrm{A}}^{\dagger} \tag{95a}$$

$$\vec{\hat{a}}^{(1)} = \underline{\mathrm{A}}^{\dagger}(\omega)\vec{\hat{a}}^{(2)} := \hat{\mathrm{A}}^{\dagger}\vec{\hat{a}}^{(1)}\hat{\mathrm{A}}. \tag{95b}$$

In an ideal AWG, different wavelengths of an input field exit from different output waveguides. Hence,

$$|\mathrm{A}_{ji}(\omega)|^2 \approx \begin{cases} 1, & |\omega - \omega_{ji}| \le \Delta\omega_{\mathrm{A}}/2 \\ 0, & \text{otherwise} \end{cases} \tag{96}$$

where $\Delta\omega_{\mathrm{A}}$ is the AWG bandwidth.

Fig. 11 shows a 4×4 AWG that guides four frequencies in its output ports based on the frequency received from each input port. On-chip schemes of the arrayed WGR in C-, S-, L-, and O-band frequencies, as a device with low-latency and nonblocking interconnection, were implemented successfully [58], [66], [67].

A. DEMULTIPLEXING

Fig. 12(a) illustrates an example of wavelength multiplexing in a 4×4 AWG, where a broadband signal launches into its third input port. Consider the broadband wave-packet $\zeta_3(\omega)$ corresponding to the input creation operator $\hat{a}^{\dagger(1)}_{3,\zeta_3}$ including

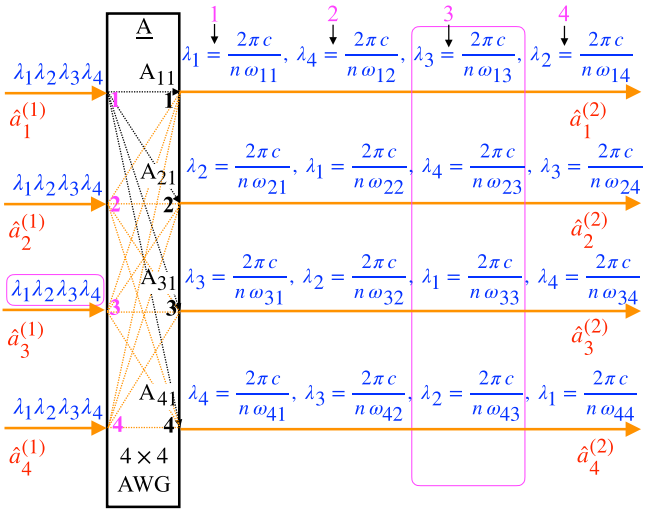

FIGURE 11. 4 × 4 AWG, which can be used as a WGR.

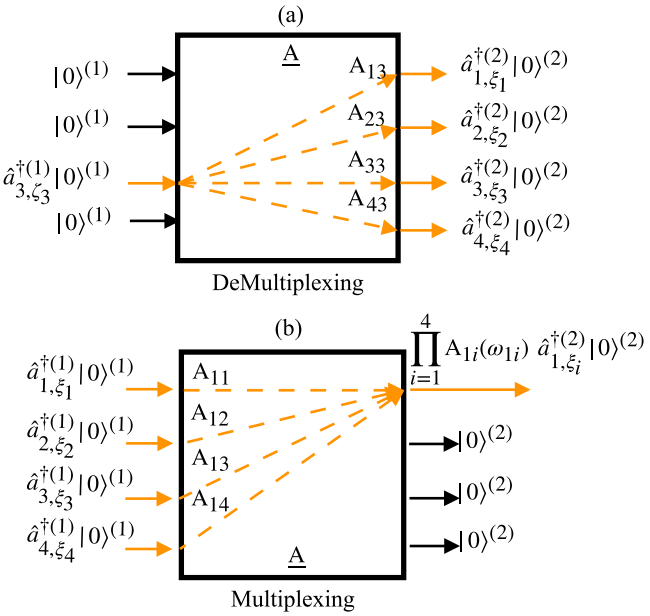

FIGURE 12. (a) Demultiplexing and (b) multiplexing setup of a 4 × 4 AWG.

the sum of the narrowband spectrum profiles such that

$$\hat{a}^{\dagger(1)}_{3,\xi_3} = \int d\omega \zeta_3(\omega)\hat{a}^{\dagger(1)}_3(\omega) = \int d\omega \sum_{n=1}^{4} c_n \xi_n(\omega)\hat{a}^{\dagger(1)}_3(\omega) \tag{97}$$

where c_n is the normalized weight amplitude ($\sum_{n=1}^{4}|c_n|^2 = 1$), and

$$\xi_n(\omega) = \frac{1}{\sqrt{\pi}\sigma} e^{[-\frac{(\omega-\omega_{n3})^2}{2\sigma^2}]}\ \forall n, n' \in \{1,\ldots,4\}, \sigma \ll \omega_{n3} - \omega_{n'3}$$

is the normalized Gaussian narrowband function.

Since $\int \xi_n^*(\omega)\xi_{n'}(\omega)d\omega = \delta_{nn'}$, the wave-packet $\xi_n(\omega_{n'3}) \approx 0\,(n \neq n')\ \forall n, n' \in \{1,\ldots,4\}$, where ω_{n3} is the guided frequency from port 3 to n. Moreover, $A_{j3}(\omega) \neq 0$, where $|\omega - \omega_{j3}| \leq \Delta\omega_A/2$. Therefore, considering the condition $\Delta\omega_A \geq \sigma$ while $A_{j3}(\omega)$ is almost constant and nonzero along the width of $\xi_j(\omega)$, the approximation $\xi_n(\omega)A_{j3}(\omega) \approx \delta_{nj}\xi_n(\omega)A_{j3}(\omega_{j3})$ is taken into account.

Using (94), the input creation operator given in (97) is rewritten based on the output creation operator as

$$\begin{aligned}\hat{a}^{\dagger(1)}_{3,\zeta_3} &= \sum_n c_n \int d\omega \xi_n(\omega) \sum_j A_{j3}(\omega)\hat{a}^{\dagger(2)}_j(\omega) \\ &\approx \sum_n c_n \int d\omega \sum_j \delta_{nj}\xi_n(\omega)A_{j3}(\omega_{j3})\hat{a}^{\dagger(2)}_j(\omega) \\ &= \sum_j c_j A_{j3}(\omega_{j3}) \int d\omega \xi_j(\omega)\hat{a}^{\dagger(2)}_j(\omega) \\ &= \sum_j c_j A_{j3}(\omega_{j3})\hat{a}^{\dagger(2)}_{j,\xi_j}.\end{aligned} \tag{98}$$

Equation (98) describes the demultiplexing functionality of the AWG. For a more general case, the creation operator $\hat{a}^{\dagger(1)}_{i,\zeta} = \int d\omega\zeta(\omega)\hat{a}^{\dagger(1)}_i(\omega)$ with arbitrary wave-packet $\zeta(\omega)$ is entered into the ith input. The input operators related to the ith port are rewritten based on the output operators related to different output ports as

$$\hat{a}^{(1)}_{i,\zeta} = \sum_{j=1}^{N} \int d\omega\zeta(\omega)A_{ji}(\omega)\hat{a}^{\dagger(2)}_j(\omega) \tag{99}$$

where $A_{ji}(\omega)$ according to (96) acts as a filter around the frequency ω_{ji}.

B. MULTIPLEXING

As shown in Fig. 12(b), consider each input of the AWG is fed by a single-photon narrowband wave-packet $\xi_i(\omega)$ with the carrier frequency ω_i. So, the overall input is written as follows:

$$|\psi\rangle^{(1)} = \prod_{i=1}^{N} \int d\omega \xi_i(\omega)\hat{a}^{\dagger(1)}_i(\omega)|0\rangle^{(1)}. \tag{100}$$

Assuming the central frequency of ξ_i is $\omega_i = \omega_{1i}$ where ω_{1i} is the guided frequency of AWG from input i to output 1, by use of (94) and (96) the state in the output port number 1 contains all the input modes as follows:

$$\begin{aligned}|\psi\rangle^{(2)} &= \prod_{i=1}^{N} \int d\omega \xi_i(\omega) \sum_j A_{ji}(\omega)\hat{a}^{\dagger(2)}_j(\omega)|0\rangle^{(2)} \\ &\approx \prod_{i=1}^{N} \int d\omega \sum_j \delta_{j1}\xi_i(\omega)A_{ji}(\omega_{1i})\hat{a}^{\dagger(2)}_j(\omega)|0\rangle^{(2)} \\ &\approx \prod_{i=1}^{N} A_{1i}(\omega_{1i})\hat{a}^{\dagger(2)}_{1,\xi_i}|0\rangle^{(2)}\end{aligned} \tag{101}$$

IEEE Transactions on Quantum Engineering

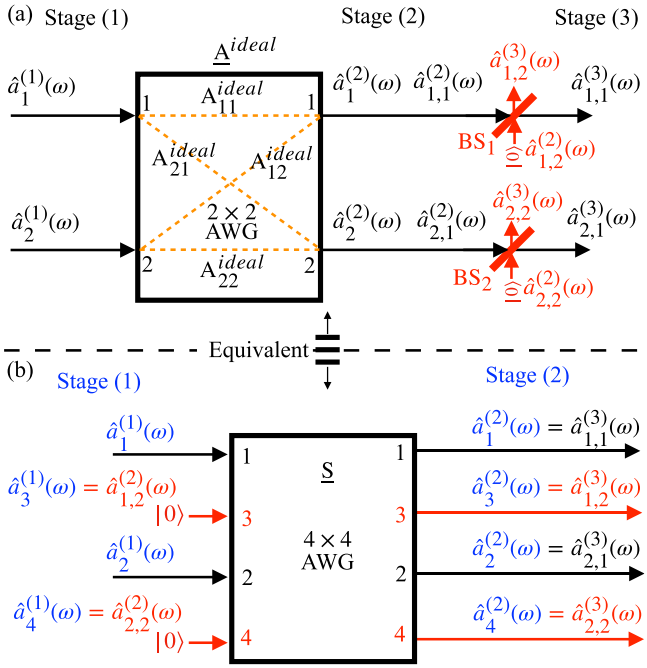

FIGURE 13. (a) Schematic configuration of a 2 × 2 lossy AWG modeled by a lossless 2 × 2 AWG ($\underline{\mathrm{A}}^{\mathrm{ideal}}$) followed by frequency-dependent beam splitters (BS_1 and BS_2). (b) Schematic configuration of a unitary 4 × 4 transfer matrix $\underline{\mathrm{S}}$ which is equivalent to (a).

where $\xi_i(\omega)\mathrm{A}_{ji}(\omega) \approx \delta_{j1}\xi_i(\omega)\mathrm{A}_{ji}(\omega_{1i})$ and it is assumed the bandwidth of $\xi_i(\omega)$ is less than the AWG bandwidth. Neglecting crosstalk, all the other output states are vacuum states. This is the multiplexing procedure. Note that in an ideal AWG, A_{1i} is only a phase term [see (96)].

C. LOSS EFFECTS

For a lossy AWG, ambient degrees of freedom (dielectric medium), which consume some part of the energy of the input field, must be considered. Due to the conservation of energy

$$\sum_j |E_j^{\mathrm{out}}(\omega)|^2 = \sum_j \left|\sum_i \mathrm{A}_{ji}(\omega)E_i^{\mathrm{in}}(\omega)\right|^2 \le \sum_i |E_i^{\mathrm{in}}(\omega)|^2$$

where $E_i^{\mathrm{in}}(\omega)$ ($E_j^{\mathrm{out}}(\omega)$) is the electric field of input (output) mode of ith (jth) waveguide. Therefore, the eigenvalues of the coefficient matrix $\underline{\mathrm{A}}$ must be equal to or less than one.

To model the environmental effect, which leads to a loss, we first investigate a 2 × 2 AWG. As illustrated in Fig. 13, a lossy 2 × 2 AWG can be realized as an ideal AWG ($\underline{\mathrm{A}}^{\mathrm{ideal}}$), where each output passes through a lossless BS with a frequency-dependent transmission coefficient. Hence, a 4 × 4 unitary matrix represented by $\underline{\mathrm{S}}$ becomes a mathematical model for a lossy 2 × 2 AWG. The absolute values of matrix elements of an ideal AWG are one or zero. Transmission coefficients of BSs as a loss model equal transmission coefficients of a lossy AWG for each frequency ω. The transmission and reflection coefficients of the frequency-dependent symmetric BSs ($\mathrm{B}_{j,11}(\omega) = \mathrm{B}_{j,22}(\omega)$ and $\mathrm{B}_{j,12}(\omega) = \mathrm{B}_{j,21}(\omega)$) existing in the unitary $\underline{\mathrm{S}}$ as a loss model of a 2 × 2 lossy AWG (see Fig. 13), are chosen as follows:

$$\begin{aligned}
&\mathrm{B}_{1,11}(\omega_1) = \tilde{\mathrm{A}}_{11}(\omega_1),\ \mathrm{B}_{1,21}(\omega_1) = i\sqrt{1-\mathrm{A}_{11}^*(\omega_1)\mathrm{A}_{11}(\omega_1)}\\
&\mathrm{B}_{1,11}(\omega_2) = \tilde{\mathrm{A}}_{12}(\omega_2),\ \mathrm{B}_{1,21}(\omega_2) = i\sqrt{1-\mathrm{A}_{12}^*(\omega_2)\mathrm{A}_{12}(\omega_2)}\\
&\mathrm{B}_{1,12}(\omega_1) = i\sqrt{1-\mathrm{A}_{11}^*(\omega_1)\mathrm{A}_{11}(\omega_1)},\ \mathrm{B}_{1,22}(\omega_1) = \tilde{\mathrm{A}}_{11}(\omega_1)\\
&\mathrm{B}_{1,12}(\omega_2) = i\sqrt{1-\mathrm{A}_{12}^*(\omega_2)\mathrm{A}_{12}(\omega_2)},\ \mathrm{B}_{1,22}(\omega_2) = \tilde{\mathrm{A}}_{12}(\omega_2)\\
&\mathrm{B}_{2,11}(\omega_1) = \tilde{\mathrm{A}}_{22}(\omega_1),\ \mathrm{B}_{2,12}(\omega_1) = i\sqrt{1-\mathrm{A}_{22}^*(\omega_1)\mathrm{A}_{22}(\omega_1)}\\
&\mathrm{B}_{2,11}(\omega_2) = \tilde{\mathrm{A}}_{21}(\omega_2),\ \mathrm{B}_{2,12}(\omega_2) = i\sqrt{1-\mathrm{A}_{21}^*(\omega_2)\mathrm{A}_{21}(\omega_2)}\\
&\mathrm{B}_{2,21}(\omega_1) = i\sqrt{1-\mathrm{A}_{22}^*(\omega_1)\mathrm{A}_{22}(\omega_1)},\ \mathrm{B}_{2,22}(\omega_1) = \tilde{\mathrm{A}}_{22}(\omega_1)\\
&\mathrm{B}_{2,21}(\omega_2) = i\sqrt{1-\mathrm{A}_{21}^*(\omega_2)\mathrm{A}_{21}(\omega_2)},\ \mathrm{B}_{2,22}(\omega_2) = \tilde{\mathrm{A}}_{21}(\omega_2)
\end{aligned} \tag{102}$$

where $\tilde{\mathrm{A}}_{ij} = \mathrm{A}_{ij}e^{-i\phi_{ij}^a}$ and ϕ_{ij}^a is the phase introduced in the path $i-j$ of an ideal AWG. Note that, in (102), it is assumed $\omega_{11} = \omega_{22} = \omega_1$ and $\omega_{12} = \omega_{21} = \omega_2$. In a general case, a lossy $N \times N$ AWG is modeled by a lossless (ideal) $N \times N$ AWG accompanied by N BSs, each of them is put in each output of the lossless AWG. By use of (93), the input–output mode relationships of an ideal $N \times N$ AWG and N seperate 2 × 2 frequency-dependent BSs BS_i $i \in \{1, \ldots, N\}$ are given, respectively, by

$$\hat{a}_j^{(2)}(\omega) = \sum_{i=1}^{N} \mathrm{A}_{ji}^{\mathrm{ideal}}(\omega)\hat{a}_i^{(1)}(\omega) \tag{103}$$

$$\hat{a}_{j,l}^{(3)}(\omega) = \sum_{s=1}^{2} \mathrm{B}_{j,ls}(\omega)\hat{a}_{j,s}^{(2)}(\omega). \tag{104}$$

It may be helpful to mention that the generalized form of Fig. 13 resembles Fig. 1 related to a general quantum WDM communication system, where frequency-dependent BSs are substituted for quantum receivers' operators. Thus, $\hat{a}_j^{(2)}(\omega) \equiv \hat{a}_{j,1}^{(2)}(\omega)$ where $s = 1$. After inserting (103) into (104), the output modes at stage (3) (after BSs) are rewritten as

$$\hat{a}_{j,l}^{(3)}(\omega) = \mathrm{B}_{j,l1}(\omega)\sum_{i=1}^{N} \mathrm{A}_{ji}^{\mathrm{ideal}}(\omega)\hat{a}_i^{(1)}(\omega) + \mathrm{B}_{j,l2}(\omega)\hat{a}_{j,2}^{(2)}(\omega). \tag{105}$$

Therefore, a lossy $N \times N$ AWG is modeled by a $2N \times 2N$ unitary matrix which is identified by the transfer matrix $\underline{\mathrm{S}}$

which relates input modes to outputs as

$$\vec{\hat{a}}^{(2)}(\omega) = \underline{\mathrm{S}}_{2N\times 2N}\vec{\hat{a}}^{(1)}(\omega) \tag{106}$$

where

$$\vec{\hat{a}}^{(1)}(\omega) = (\hat{a}_1^{(1)}(\omega), \ldots, \hat{a}_{2N}^{(1)}(\omega))^{\mathrm{T}}$$
$$\vec{\hat{a}}^{(2)}(\omega) = (\hat{a}_1^{(2)}(\omega), \ldots, \hat{a}_{2N}^{(2)}(\omega))^{\mathrm{T}}$$

and the elements of $\underline{\mathrm{S}}$ is specified by (105).

For instance, the $\underline{\mathrm{S}}$ corresponding to a 2×2 lossy AWG depicted in Fig. 13 becomes (107), shown at the bottom of this page. If $\omega_{11} = \omega_{22} = 2\pi c/\lambda_1$ and $\omega_{12} = \omega_{21} = 2\pi c/\lambda_2$, $\underline{\mathrm{A}}^{\mathrm{ideal}}(\omega_1)$ and $\underline{\mathrm{A}}^{\mathrm{ideal}}(\omega_2)$ are unitary matrices look like the following forms:

$$\underline{\mathrm{A}}^{\mathrm{ideal}}(\omega_1) = \begin{bmatrix} e^{i\phi_{11}^a} & 0 \\ 0 & e^{i\phi_{22}^a} \end{bmatrix}$$
$$\underline{\mathrm{A}}^{\mathrm{ideal}}(\omega_2) = \begin{bmatrix} 0 & e^{i\phi_{12}^a} \\ e^{i\phi_{21}^a} & 0 \end{bmatrix}$$

where ϕ_{ij}^a is the phase introduced in the path $i-j$ of an ideal AWG. The lossy 2×2 AWG is written as [45]

$$\underline{\mathrm{A}}^{lossy}(\omega) = \begin{bmatrix} \mathrm{A}_{11}(\omega) & \mathrm{A}_{12}(\omega) \\ \mathrm{A}_{21}(\omega) & \mathrm{A}_{22}(\omega) \end{bmatrix}$$

where

$$|\mathrm{A}_{11}(\omega_1)| \le 1,\ \mathrm{A}_{11}(\omega \notin (\omega_1 - \Delta\omega_A/2, \omega_1 + \Delta\omega_A/2))) \approx 0$$
$$|\mathrm{A}_{22}(\omega_1)| \le 1,\ \mathrm{A}_{22}(\omega \notin (\omega_1 - \Delta\omega_A/2, \omega_1 + \Delta\omega_A/2))) \approx 0$$
$$|\mathrm{A}_{12}(\omega_2)| \le 1,\ \mathrm{A}_{12}(\omega \notin (\omega_2 - \Delta\omega_A/2, \omega_2 + \Delta\omega_A/2))) \approx 0$$
$$|\mathrm{A}_{21}(\omega_2)| \le 1,\ \mathrm{A}_{21}(\omega \notin (\omega_2 - \Delta\omega_A/2, \omega_2 + \Delta\omega_A/2))) \approx 0.$$

As a result, according to (102) and (107), the unitary matrix $\underline{\mathrm{S}}_{4\times 4}$ in the frequency ω_1 and ω_2 become (108) and (109), shown at the bottom of this page.

It is important to note that two extra input modes $\hat{a}_{1,2}^{(2)}(\omega)$ and $\hat{a}_{2,2}^{(2)}(\omega)$ are in charge of adding noise to the system due to the interaction of light and medium. The minimum noise that arises from this model is related to vacuum noise for each extra-added input mode in the BS.

Since, according to (85), the transmission coefficient is sensitive more to frequency than the number of input–output waveguides ($N_{in} = N_o$), increasing the number of users does not significantly change the amount of loss in each channel. Based on this claim, the lossy model presented in Fig. 13 is designed.

D. CROSSTALK EFFECTS

In the real world, for an actual AWG, indeed, there is a narrow frequency band $\Delta\omega_A$ around the central value ω_{ji} of each output channel in which $|\mathrm{A}_{ji}(\omega \notin (\omega_{ji} - \Delta\omega_A/2, \omega_{ji} + \Delta\omega_A/2))|^2 \ll 1$. The frequency space between two adjacent channels is indicated by $\Delta\omega_c$, which is adjusted more than the frequency band $\Delta\omega_A$. The existence of a finite band for the passing mode introduces two kinds of crosstalk effects: 1) out-of-band cross-talks and 2) in-band cross-talks. The former is related to the contribution of the energy related to frequencies that are different from the desired channel frequency. The out-of-band crosstalk is usually omitted by proper filtering. However, the filters will not vanish the in-band crosstalk, which is associated with the energy of the same frequency as the channel frequency that arises from the adjacent channels.

$$\underline{\mathrm{S}}_{4\times 4}(\omega) = \begin{bmatrix} \mathrm{B}_{1,11}(\omega)\mathrm{A}_{11}^{\mathrm{ideal}}(\omega) & \mathrm{B}_{1,11}(\omega)\mathrm{A}_{12}^{\mathrm{ideal}}(\omega) & \mathrm{B}_{1,12}(\omega) & 0 \\ \mathrm{B}_{2,11}(\omega)\mathrm{A}_{21}^{\mathrm{ideal}}(\omega) & \mathrm{B}_{2,11}(\omega)\mathrm{A}_{22}^{\mathrm{ideal}}(\omega) & 0 & \mathrm{B}_{2,12}(\omega) \\ \mathrm{B}_{1,21}(\omega)\mathrm{A}_{11}^{\mathrm{ideal}}(\omega) & \mathrm{B}_{1,21}(\omega)\mathrm{A}_{12}^{\mathrm{ideal}}(\omega) & \mathrm{B}_{1,22}(\omega) & 0 \\ \mathrm{B}_{2,21}(\omega)\mathrm{A}_{21}^{\mathrm{ideal}}(\omega) & \mathrm{B}_{2,21}(\omega)\mathrm{A}_{22}^{\mathrm{ideal}}(\omega) & 0 & \mathrm{B}_{2,22}(\omega) \end{bmatrix} \tag{107}$$

$$\underline{\mathrm{S}}_{4\times 4}(\omega_1) = \begin{bmatrix} \mathrm{A}_{11}(\omega_1) & 0 & \mathrm{B}_{1,12}(\omega_1) & 0 \\ 0 & \mathrm{A}_{22}(\omega_1) & 0 & \mathrm{B}_{2,21}(\omega_1) \\ \mathrm{B}_{1,21}(\omega_1)e^{i\phi_{11}^a} & 0 & \mathrm{A}_{11}(\omega_1)e^{-i\phi_{11}^a} & 0 \\ 0 & \mathrm{B}_{2,21}(\omega_1)e^{i\phi_{22}^a} & 0 & \mathrm{A}_{22}(\omega_1)e^{-i\phi_{11}^a} \end{bmatrix} \tag{108}$$

$$\underline{\mathrm{S}}_{4\times 4}(\omega_2) = \begin{bmatrix} 0 & \mathrm{A}_{12}(\omega_2) & \mathrm{B}_{1,12}(\omega_2) & 0 \\ \mathrm{A}_{21}(\omega_2) & 0 & 0 & \mathrm{B}_{2,12}(\omega_2) \\ 0 & \mathrm{B}_{1,21}(\omega_2)e^{i\phi_{12}^a} & \mathrm{A}_{12}(\omega_2)e^{-i\phi_{12}^a} & 0 \\ \mathrm{B}_{2,21}(\omega_2)e^{i\phi_{21}^a} & 0 & 0 & \mathrm{A}_{21}(\omega_2)e^{-i\phi_{21}^a} \end{bmatrix} \tag{109}$$

IEEE Transactions on Quantum Engineering

According to (93), the outputs of the AWG when the ith input port is fed are

$$\hat{\mathrm{A}}^{\dagger}\hat{a}_i^{(1)}(\omega_{ji})\hat{\mathrm{A}} = \mathrm{A}_{1i}^{*}(\omega_{ji})\hat{a}_1^{(2)}(\omega_{ji}) + \cdots + \mathrm{A}_{j-1,i}^{*}(\omega_{ji})\hat{a}_{j-1}^{(2)}(\omega_{ji}) + \mathrm{A}_{ji}^{*}(\omega_{ji})\hat{a}_j^{(2)}(\omega_{ji}) + \mathrm{A}_{j+1,i}^{*}(\omega_{ji})\hat{a}_{j+1}^{(2)}(\omega_{ji}) + \cdots + \mathrm{A}_{Ni}^{*}(\omega_{ji})\hat{a}_N^{(2)}(\omega_{ji}). \quad (110)$$

If $\Delta\omega_c$ is big enough with respect to $\Delta\omega_A$ the prominent terms of crosstalk in practice are related to the values of coefficients $\mathrm{A}_{j-1,i}(\omega_{ji})$ and $\mathrm{A}_{j+1,i}(\omega_{ji})$.

REFERENCES

[1] S. Pirandola et al., "Advances in quantum cryptography," *Adv. Opt. Photon.*, vol. 12, no. 4, pp. 1012–1236, Dec. 2020, doi: 10.1364/AOP.361502.

[2] F. Cavaliere, E. Prati, L. Poti, I. Muhammad, and T. Catuogno, "Secure quantum communication technologies and systems: From labs to markets," *Quantum Rep.*, vol. 2, no. 1, pp. 80–106, 2020, doi: 10.3390/quantum2010007.

[3] G. Cariolaro, *Quantum Communications*. Berlin, Germany: Springer, 2015, doi: 10.1007/978-3-319-15600-2.

[4] S. Koudia, A. S. Cacciapuoti, K. Simonov, and M. Caleffi, "How deep the theory of quantum communications goes: Superadditivity, superactivation and causal activation," *IEEE Commun. Surveys Tut.*, vol. 24, no. 4, pp. 1926–1956, Fourth quarter 2022, doi: 10.1109/COMST.2022.3196449.

[5] M. A. Nielsen and I. Chuang, "*Quantum Computation and Quantum Information*. Cambridge, U.K.: Cambridge Univ. Press, 2002, doi: 10.1017/CBO9780511976667.

[6] D. Main et al., "Distributed quantum computing across an optical network link," *Nature*, vol. 638, pp. 383–388, 2025, doi: 10.1038/s41586-024-08404-x.

[7] T. S. Humble and W. P. Grice, "Spectral effects in quantum teleportation," *Phys. Rev. A*, vol. 75, Feb. 2007, Art. no. 022307, doi: 10.1103/PhysRevA.75.022307.

[8] J. M. Thomas et al., "Quantum teleportation coexisting with classical communications in optical fiber," *Optica*, vol. 11, no. 12, pp. 1700–1707, Dec. 2024, doi: 10.1364/OPTICA.540362.

[9] J. Liu, M. Zhang, H. Chen, L. Wang, and H. Yuan, "Optimal scheme for quantum metrology," *Adv. Quantum Technol.*, vol. 5, no. 1, 2022, Art. no. 2100080, doi: 10.1002/qute.202100080.

[10] G. Vardoyan and S. Wehner, "Quantum network utility maximization," 2022, *arXiv:2210.08135*, doi: 10.48550/arXiv.2210.08135.

[11] H. Zhou, K. Lv, L. Huang, and X. Ma, "Quantum network: Security assessment and key management," *IEEE/ACM Trans. Netw.*, vol. 30, no. 3, pp. 1328–1339, Jun. 2022, doi: 10.1109/TNET.2021.313694.

[12] A. S. Cacciapuoti, M. Caleffi, R. Van Meter, and L. Hanzo, "When entanglement meets classical communications: Quantum teleportation for the quantum internet," *IEEE Trans. Commun.*, vol. 68, no. 6, pp. 3808–3833, Jun. 2020, doi: 10.1109/TCOMM.2020.297807.

[13] M. Bathaee, M. Rezai, and J. A. Salehi, "Quantum wavelength-division-multiplexing and multiple-access communication systems and networks: Global and unified approach," *Phys. Rev. A*, vol. 107, Jan. 2023, Art. no. 012613, doi: 10.1103/PhysRevA.107.012613.

[14] D. Chadha, *Optical WDM Networks: From Static to Elastic Networks*. Hoboken, NJ, USA: Wiley, 2019, doi: 10.1002/9781119393399.

[15] G. P. Agrawal, *Fiber-Optic Communication Systems*, 5th ed., Hoboken, NJ, USA: Wiley, 2021, doi: 10.1002/9781119737391.

[16] M. S. Goodman, H. Kobrinski, M. P. Vecchi, R. M. Bulley, and J. L. Gimlett, "The LAMBDANET multiwavelength network: Architecture, applications, and demonstrations," *IEEE J. Sel. Areas Commun.*, vol. 8, no. 6, pp. 995–1004, Aug. 1990, doi: 10.1109/49.57802.

[17] S. Wang et al., "Field test of wavelength-saving quantum key distribution network," *Opt. Lett.*, vol. 35, no. 14, pp. 2454–2456, Jul. 2010, doi: 10.1364/OL.35.002454.

[18] I. Choi, R. J. Young, and P. D. Townsend, "Quantum key distribution on a 10gb/s WDM-PON," *Opt. Exp.*, vol. 18, no. 9, pp. 9600–9612, 2010, doi: 10.1364/OE.18.009600.

[19] B. Fröhlich, J. F. Dynes, M. Lucamarini, A. W. Sharpe, Z. Yuan, and A. J. Shields, "A quantum access network," *Nature*, vol. 501, no. 7465, pp. 69–72, 2013, doi: 10.1038/nature12493.

[20] X. Yu et al., "Multi-dimensional routing, wavelength, and timeslot allocation (RWTA) in quantum key distribution optical networks (QKD-ON)," *Appl. Sci.*, vol. 11, no. 1, 2021, Art. no. 348, doi: 10.3390/app11010348.

[21] X.-Y. Zhou, J.-R. Hu, J.-J. Wang, Y. Cao, C.-H. Zhang, and Q. Wang, "Enhancing the performance of mode-pairing quantum key distribution by wavelength division multiplexing," *Opt. Exp.*, vol. 32, no. 10, pp. 18366–18378, May 2024, doi: 10.1364/OE.519591.

[22] M. Kim et al., "Free-space quantum key distribution transmitter system using WDM filter for channel integration," *ETRI J.*, vol. 46, no. 5, pp. 806–816, 2024, doi: 10.4218/etrij.2024-0142.

[23] J. Mora et al., "Simultaneous transmission of 20 x 2 WDM/SCM-QKD and 4 bidirectional classical channels over a PON," *Opt. Exp.*, vol. 20, no. 15, pp. 16358–16365, 2012, doi: 10.1364/OE.20.016358.

[24] L.-J. Wang et al., "Experimental multiplexing of quantum key distribution with classical optical communication," *Appl. Phys. Lett.*, vol. 106, no. 8, 2015, Art. no. 081108, doi: 10.1063/1.4913483.

[25] K. Patel et al., "Quantum key distribution for 10 gb/s dense wavelength division multiplexing networks," *Appl. Phys. Lett.*, vol. 104, no. 5, 2014, Art. no. 051123, doi: 10.1063/1.4864398.

[26] K. Patel et al., "Coexistence of high-bit-rate quantum key distribution and data on optical fiber," *Phys. Rev. X*, vol. 2, no. 4, 2012, Art. no. 041010, doi: 10.1103/PhysRevX.2.041010.

[27] T. Chapuran et al., "Optical networking for quantum key distribution and quantum communications," *New J. Phys.*, vol. 11, no. 10, 2009, Art. no. 105001, doi: 10.1088/1367-2630/11/10/105001.

[28] A. Bahrami, A. Lord, and T. Spiller, "Quantum key distribution integration with optical dense wavelength division multiplexing: A review," *IET Quantum Commun.*, vol. 1, no. 1, pp. 9–15, 2020, doi: 10.1049/iet-qtc.2019.0005.

[29] E. Udvary, "Integration of QKD channels to classical high-speed optical communication networks," *Infocommunications J.*, vol. 15, no. 4, pp. 2–9, 2023, doi: 10.36244/ICJ.2023.4.1.

[30] L. Ruiz and J. C. Garcia-Escartin, "Routing and wavelength assignment in hybrid networks with classical and quantum signals," *IEEE J. Sel. Areas Commun.*, vol. 43, no. 2, pp. 412–421, Feb. 2025, doi: 10.1109/JSAC.2025.3528817.

[31] S. Chaudhary, S. Dehdashti, I. Litvin, and J. Nötzel, "Robustness of WDM technique for the co-propagation of quantum-with classical signals in an optical fiber," 2024, *arXiv:2411.16942*, doi: 10.48550/arXiv.2411.16942.

[32] S. Bahrani, M. Razavi, and J. A. Salehi, "Wavelength assignment in hybrid quantum-classical networks," *Sci. Rep.*, vol. 8, no. 1, 2018, Art. no. 3456, doi: 10.1038/s41598-018-21418-6.

[33] S. Bahrani, M. Razavi, and J. A. Salehi, "Crosstalk reduction in hybrid quantum-classical networks," *Scientia Iranica*, vol. 23, no. 6, pp. 2898–2907, 2016, doi: 10.24200/sci.2016.3999.

[34] A. Ciurana et al., "Quantum metropolitan optical network based on wavelength division multiplexing," *Opt. Exp.*, vol. 22, no. 2, pp. 1576–1593, 2014, doi: 10.1364/OE.22.001576.

[35] A. Ciurana, V. Martin, J. Martinez-Mateo, B. Schrenk, M. Peev, and A. Poppe, "Entanglement distribution in optical networks," *IEEE J. Sel. Topics Quantum Electron.*, vol. 21, no. 3, May/Jun. 2015, Art. no. 6400212, doi: 10.1109/JSTQE.2014.2367241.

[36] M. Bathaee and J. A. Salehi, "Entangled-based quantum wavelength-division-multiplexing and multiple-access networks," *Entropy*, vol. 25, no. 12, 2023, doi: 1099-4300/25/12/1658.

[37] G. Liu et al., "Single-photon generation and manipulation in quantum nanophotonics," *Appl. Phys. Rev.*, vol. 12, no. 1, 2025, Art. no. 011308, doi: 10.1063/5.0227350.

[38] W. Luo et al., "Recent progress in quantum photonic chips for quantum communication and internet," *Light: Sci. Appl.*, vol. 12, no. 1, 2023, Art. no. 175, doi: 10.1038/s41377-023-01173-8.

[39] N. Gisin, G. Ribordy, W. Tittel, and H. Zbinden, "Quantum cryptography," *Rev. Modern Phys.*, vol. 74, no. 1, 2002, Art. no. 145, doi: 10.1103/RevModPhys.74.145.

[40] M. Rezai and J. A. Salehi, "Quantum CDMA communication systems," *IEEE Trans. Inf. Theory*, vol. 67, no. 8, pp. 5526–5547, Aug. 2021, doi: 10.1109/TIT.2021.3087959.

[41] P. D. Townsend, "Quantum cryptography on multiuser optical fibre networks," *Nature*, vol. 385, no. 6611, pp. 47–49, 1997, doi: 10.1038/385047a0.

[42] P. L. Kelley and W. H. Kleiner, "Theory of electromagnetic field measurement and photoelectron counting," *Phys. Rev.*, vol. 136, pp. A316–A334, Oct. 1964, doi: 10.1103/PhysRev.136.A316.

[43] X. Ma, B. Qi, Y. Zhao, and H.-K. Lo, "Practical decoy state for quantum key distribution," *Phys. Rev. A*, vol. 72, Jul. 2005, Art. no. 012326, doi: 10.1103/PhysRevA.72.012326.

[44] C. M. Caves, "Quantum limits on noise in linear amplifiers," *Phys. Rev. D*, vol. 26, pp. 1817–1839, Oct. 1982, doi: 10.1103/PhysRevD.26.1817.

[45] J. Capmany, J. Mora, C. R. Fernández-Pousa, and P. Muñoz, "Quantum model of light transmission in array waveguide gratings," *Opt. Exp.*, vol. 21, no. 12, pp. 14841–14852, 2013, doi: 10.1364/OE.21.014841.

[46] P. Munoz, D. Pastor, and J. Capmany, "Modeling and design of arrayed waveguide gratings," *J. Lightw. Technol.*, vol. 20, no. 4, pp. 661–674, Apr. 2002, doi: 10.1109/50.996587.

[47] N. Jain, B. Stiller, I. Khan, D. Elser, C. Marquardt, and G. Leuchs, "Attacks on practical quantum key distribution systems (and how to prevent them)," *Contemporary Phys.*, vol. 57, no. 3, pp. 366–387, 2016, doi: 10.1080/00107514.2016.1148333.

[48] C. Bennett, G. Brassard, C. Crepeau, and U. Maurer, "Generalized privacy amplification," *IEEE Trans. Inf. Theory*, vol. 41, no. 6, pp. 1915–1923, Nov. 1995, doi: 10.1109/18.476316.

[49] A. Duplinskiy, V. Ustimchik, A. Kanapin, V. Kurochkin, and Y. Kurochkin, "Low loss QKD optical scheme for fast polarization encoding," *Opt. Exp.*, vol. 25, no. 23, pp. 28886–28897, 2017, doi: 10.1364/OE.25.028886.

[50] K. Lim, H. Ko, C. Suh, and J.-K. K. Rhee, "Security analysis of quantum key distribution on passive optical networks," *Opt. Exp.*, vol. 25, no. 10, pp. 11894–11909, 2017, doi: 10.1364/OE.25.011894.

[51] M. Rezai and J. A. Salehi, "Fundamentals of quantum Fourier optics," *IEEE Trans. Quantum Eng.*, vol. 4, 2023, Art. no. 2100122, doi: 10.1109/TQE.2022.3224799.

[52] R. J. Donaldson, L. Mazzarella, R. J. Collins, J. Jeffers, and G. S. Buller, "A high-gain and high-fidelity coherent state comparison amplifier," *Commun. Phys.*, vol. 1, no. 1, p. 54, 2018, doi: 10.1038/s42005-018-0054-z.

[53] M. Bathaee, N. Marjan, and A. R. Bahrampour, "Feedforward-assisted coherent-state comparison amplifier," *Phys. Rev. A*, vol. 100, Oct. 2019, Art. no. 043809, doi: 10.1103/PhysRevA.100.043809.

[54] A. A. Gaidash, V. I. Egorov, and A. V. Gleim, "Revealing of photon-number splitting attack on quantum key distribution system by photon-number resolving devices," *J. Phys.: Conf. Ser.*, vol. 735, no. 1, Aug. 2016, Art. no. 012072, doi: 10.1088/1742-6596/735/1/012072.

[55] P. W. Shor and J. Preskill, "Simple proof of security of the BB84 quantum key distribution protocol," *Phys. Rev. Lett.*, vol. 85, pp. 441–444, Jul. 2000, doi: 10.1103/PhysRevLett.85.441.

[56] N. J. Beaudry, T. Moroder, and N. Lütkenhaus, "Squashing models for optical measurements in quantum communication," *Phys. Rev. Lett.*, vol. 101, Aug. 2008, Art. no. 093601, doi: 10.1103/PhysRevLett.101.093601.

[57] B. Qi, "Bennett-brassard 1984 quantum key distribution using conjugate homodyne detection," *Phys. Rev. A*, vol. 103, Jan. 2021, Art. no. 012606, doi: 10.1103/PhysRevA.103.012606.

[58] S. Pitris et al., "Silicon photonic 8 × 8 cyclic arrayed waveguide grating router for o-band on-chip communication," *Opt. Exp.*, vol. 26, no. 5, pp. 6276–6284, 2018, doi: 10.1364/OE.26.006276.

[59] H. Fearn and R. Loudon, "Quantum theory of the lossless beam splitter," *Opt. Commun.*, vol. 64, no. 6, pp. 485–490, 1987, doi: 10.1016/0030-4018(87)90275-6.

[60] A. Zeilinger, "General properties of lossless beam splitters in interferometry," *Amer. J. Phys.*, vol. 49, no. 9, pp. 882–883, 1981, doi: 10.1119/1.12387.

[61] U. Leonhardt, "Quantum physics of simple optical instruments," *Rep. Prog. Phys.*, vol. 66, no. 7, 2003, Art. no. 1207, doi: 10.1088/0034-4885/66/7/203.

[62] B. Huttner and S. M. Barnett, "Quantization of the electromagnetic field in dielectrics," *Phys. Rev. A*, vol. 46, pp. 4306–4322, Oct. 1992, doi: 10.1103/PhysRevA.46.4306.

[63] S. M. Barnett, J. Jeffers, A. Gatti, and R. Loudon, "Quantum optics of lossy beam splitters," *Phys. Rev. A*, vol. 57, pp. 2134–2145, Mar. 1998, doi: 10.1103/PhysRevA.57.2134.

[64] R. Uppu, T. A. W. Wolterink, T. B. H. Tentrup, and P. W. H. Pinkse, "Quantum optics of lossy asymmetric beam splitters," *Opt. Exp.*, vol. 24, no. 15, pp. 16440–16449, Jul. 2016, doi: 10.1364/OE.24.016440. [Online]. Available: http://opg.optica.org/oe/abstract.cfm?URI=oe-24-15-16440

[65] R. Matloob, R. Loudon, S. M. Barnett, and J. Jeffers, "Electromagnetic field quantization in absorbing dielectrics," *Phys. Rev. A*, vol. 52, pp. 4823–4838, Dec. 1995, doi: 10.1103/PhysRevA.52.4823.

[66] G. Chen, J. Zou, T. Lang, and J. He, "Compact 4 x 4 1250 GHz silicon arrayed waveguide grating router for optical interconnects," *Proc. SPIE*, vol. 9367, 2015, Art. no. 936717, doi: 10.1117/12.2078047.

[67] G. Song, J. Zou, and J. He, "Ultra-compact silicon-arrayed waveguide grating routers for optical interconnect systems," *Chin. Opt. Lett.*, vol. 15, no. 3, 2017, Art. no. 030603, doi: 10.3788/COL201715.030603.

Marzieh Bathaee was born in Tehran, Iran, in 1985. She received the B.Sc., M.Sc., and Ph.D. degrees in physics from the Sharif University of Technology, Tehran, in 2007, 2009, and 2016, respectively.

Her Ph.D. research focused on quantum optomechanics, including 3-D trapping and cooling of nanoparticles and optimal control of quantum heat engines. She has held postdoctoral research positions with the Quantum Optics and Quantum Communication Laboratory and the Sharif Quantum Center, Tehran, where she worked on quantum communication protocols, quantum thermodynamics, and quantum wavelength-division multiplexing (QWDM) networks. Her recent work includes the design and analysis of entanglement-based QWDM architectures for high-capacity quantum communication systems. She is also active in quantum machine learning, with a focus on neural network-based quantum error correction and resource optimization. Her research interests include quantum communication, quantum networks, quantum thermodynamics, quantum machine learning, and the foundations of quantum physics.

Mohammad Rezai was born in Firoozabad, Iran, in 1983. He received the B.S. degree in physics from the University of Sistan and Baluchestan, Zahedan, Iran, in 2006, the M.S. degree in physics from the Sharif University of Technology, Tehran, Iran, in 2009, and the Ph.D. degree in physics from the University of Stuttgart, Stuttgart, Germany, in 2018.

From 2010 to 2013, he was a member of the International Max Planck Research School for Advanced Materials, Munich, Germany, and part of the research staff in condensed matter physics with the Institute for Theoretical Physics III, University of Stuttgart, where he joined the 3rd Physikalisches Institut, in 2013, conducting experiments in optical quantum information processing. From 2019 to 2022, he was a postdoctoral Researcher with the Sharif Quantum Center and the Department of Electrical Engineering, Sharif University of Technology, where, since 2022, he has served as the Head of the Research Planning Department with the Sharif Quantum Center and as a faculty member of the Institute for Convergence Science and Technology. His research interests include quantum holography, quantum Fourier optics, quantum multiple-access communication systems, and quantum coherence in photosynthetic systems.

Dr. Rezai was elected to the Iran National Elite Foundation in 2019 and was the recipient of the Max Planck scholarship in 2010.

IEEE Transactions on Quantum Engineering

Jawad A. Salehi (Fellow, IEEE) was born in Kazemain, Iraq, in 1956. He received the B.Sc. degree in electrical engineering from the University of California at Irvine, Irvine, CA, USA, in 1979, and the M.Sc. and Ph.D. degrees in electrical engineering from the University of Southern California, Los Angeles, CA, USA, in 1980 and 1984, respectively.

From 1984 to 1993, he was a Member of the Technical Staff with Bell Communications Research (Bellcore), Morristown, NJ, USA. In 1990, he was a Visiting Research Scientist with the Massachusetts Institute of Technology, Cambridge, MA, USA. Since 1997, he has been a faculty member with the Sharif University of Technology (SUT), Tehran, Iran, where he is currently a Distinguished Professor, and has served as a Director of the National Center of Excellence in Communications Science and is the Founder and Head of the Optical Networks Research Laboratory and Sharif Quantum Center. He holds 15 U.S. patents. His research interests includes quantum optical signal processing, quantum CDMA, quantum Fourier optics, and optical wireless communication.

Dr. Salehi is an Fellow of OPTICA (2024), a Fellow of the Islamic World Academy of Sciences, Amman, Jordan, and a member of the Iran Academy of Science. He was the recipient of numerous national and international awards, including recognition as a Highly Cited Researcher in computer science. He was named as among the 250 preeminent and most influential researchers worldwide by the Institute for Scientific Information Highly Cited in the Computer-Science Category, 2003. He was also the recipient of the Bellcore's Award of Excellence, the Outstanding Research Award of the EE Department of SUT in 2002 and 2003, the Nationwide Outstanding Research Award 2003, and the Nation's Highly Cited Researcher Award 2004. From 2001 to 2012, he was an Associate Editor for the Optical CDMA of IEEE TRANSACTIONS ON COMMUNICATIONS. In 2024, he was elected as an OPTICA Fellow for contributions to the invention and fundamental principles of optical code-division multiple-access communication systems and of optical orthogonal codes.